Estimation of duration and its changes in Lagrangian observations relying on ice floes in the Arctic Ocean utilizing sea ice motion product

Fanyi Zhang[1,2], Ruibo Lei[1,2*], Meng Qu[2], Na Li[2], Ying Chen[2], Xiaoping Pang[1*]

[1]Chinese Antarctic Center of Surveying and Mapping, Wuhan University, Wuhan 430079, China

[2]Key Laboratory for Polar Science of the MNR, Polar Research Institute of China, Shanghai 200136, China

Correspondence to: leiruibo@pric.org.cn & pxp@whu.edu.cn

Abstract: Since the 1890s, buoy- and camp-based Lagrangian observations relying on ice floes have been indispensable for data acquisition in the difficult-to-access central Arctic Ocean in winter. Evaluating the potential observation duration and its changes associated with changes in Arctic climate system, is crucial for the planning of ice camp/buoy deployment. Using remote sensing sea ice motion product, we reconstructed sea ice drift trajectories for each annual cycle from 1979–1980 to 2022–2023 and identified the ideal areas of ice camp/buoy deployment in the central Arctic Ocean. The results show that, based on the setup time of October 1, the areas centered at 82°N and 160°E near north of the East Siberian and Laptev seas, with a size of 7.0×10^5 km^2, could ensure Lagrangian observations for at least 9 months with the drifting maintaining in the ice zone and not entering the exclusive economic zones (EEZs) of Arctic coastal countries, with the probability of 75.0%–90.9% during 44 years. The potential deployment areas favored ice advection to the Transpolar Drift (TPD) region relative to the Beaufort Gyre (BG) region. Ice trajectory terminal points did not reveal an obvious long-term tendency, but were regulated by large-scale atmospheric circulation patterns, especially the atmospheric patterns in the early drifting stage of autumn (OND). In particular, the autumn east-west surface air pressure gradient across the central Arctic and the Arctic Dipole Anomaly indices significantly influenced terminal points of ice trajectories after 9 months and can expand ideal deployment areas under scenarios with their extreme positive phases. The increasing rate of autumn–spring near-surface air temperatures along the trajectories was more pronounced in the TPD region than that in the BG region. The sea ice response to wind stress significantly intensified in recent Lagrangian observations, suggesting stronger ice dynamic processes as the sea ice thins. Geopolitical boundaries of EEZs have a significant impact on the sustainability of the Lagrangian observations, making it rarely exceed 10 months. Without this restriction, the potential Lagrangian observations in the BG and TPD regions would expand southward, with the increased duration by 20.5 and 5.0 days, respectively, compared to those with the EEZ restriction.

KEYWORDS: Arctic Ocean; Sea ice; Lagrangian observation; Buoy; Ice camp; Transpolar Drift; Beaufort Gyre

1. Introduction

Arctic sea ice, a crucial indicator and amplifier for climate change (Kwok, 2018), has experienced pronounced to become progressively thinner and younger, with its extent in September declining by 13% per decade during the satellite observation era since 1979 (Parkinson and DiGirolamo, 2021; Meier and Stroeve, 2022; Babb et al., 2023). The state-of-the-art earth system models still have an obvious spread to project the evolution of Arctic sea ice (Holland and Hunke, 2022), mainly due to insufficient observational data for parameterizations of sea ice thermodynamic and dynamic processes (Smith et al., 2022), a severe absence of reliable observation data available for assimilation (Liu et al., 2019), and the rough treatment of Arctic snow and sea ice processes by atmospheric reanalysis data (Batrak and Müller, 2019). The frozen ocean and extremely harsh weather limit the accessibility of the central Arctic Ocean, exacerbating data scarcity of ship-based oceanography measurements. This situation is even worse in the freezing season (Rabe et al., 2022).

Lagrangian measurements based on ice camp or buoy deployed on ice floes provide an alternative for the observations of interactions among atmosphere, ice, and ocean in the Arctic. In the 1890s, Fridtjof Nansen and his companions pioneered Lagrangian observations in the central Arctic Ocean using the ice camp and wooden galleon, which finally provided the first basic depiction of the Arctic sea ice and oceanic physical regimes. Subsequent ice-camp-based campaigns, including the Ice Station Alpha (Cabaniss et al., 1965), the Arctic Ice Dynamics Joint Experiment (AIDJEX; Coon, 1980), the Surface Heat Budget of the Arctic Ocean (SHEBA) campaign (Uttal et al., 2002), as well as the Norwegian young sea ICE (N-ICE2015) Expedition (Granskog et al., 2016). These efforts provided vital observation data for the construction of the theoretical framework of sea ice physics, as well as the parameterizations of sea ice thermodynamic and dynamic processes, and heat and/or salt exchanges with lower atmosphere and/or upper ocean, promoting the developing of sea ice numerical models. The Soviet Union-Russia Arctic ice-camp project, lasting for several decades since the 1930s, have provided climatological characteristics of extensive snow and sea ice geophysical variables over the central Arctic Ocean (Frolov, 2005), supporting numerical simulations (e.g., Tian et al., 2024) and remote sensing retrieval algorithms of Arctic sea ice (e.g., Lavergne et al., 2010). Recently, the Multidisciplinary drifting Observatory for the Study of the Arctic Climate (MOSAiC), fully leverages the advantages of multidisciplinary observations on the ice floes as an intermediate medium (Nicolaus et al., 2022; Rabe et al., 2022; Shupe et al., 2022), marking a milestone for Arctic drifting observation campaigns.

However, the implementation of ice camp, accompanied by a modern icebreaker as the MOSAiC, requires a significant logistical budget; or without the icebreaker supporting, as the Soviet Union-Russia ice camps, faces with risks including those from ice floe fragmentation, storms, and polar bears. These factors all limit the sustainable implementation of ice camp. It is gratifying that Arctic ice floes also provide a broad platform without the need for extra floating support for deploying

buoys or other observation instruments. Various types of buoys are designed and deployed in the Arctic Ocean to measure sea ice kinematics (Lukovich et al., 2011), snow and sea ice mass balance processes (Richter-Menge et al., 2006; Jackson et al., 2013; Nicolaus et al., 2021; Lei et al., 2022), meteorological parameters and heat exchanges over ice surface (Cox et al., 2023), as well as oceanic temperature and salinity profiles or turbulence heat flux underneath the ice (Shaw et al., 2008; Toole et al., 2011). Co-deployment of various types of buoys on the same floe to obtain comprehensive observation matrix of multiple media (e.g., Morison et al., 2002), or at a local scale of tens of kilometers (e.g., Rabe et al., 2024) to match the grid scales of satellite remote sensing (e.g., Koo et al., 2021) and numerical models (e.g., Pithan et al., 2023). Such task is extremely hard to achieve in open water.

The effective duration of Lagrangian observations relying on the ice floes, and the observation regions they may drift through, is highly dependent on the setup or deployment location of ice camp or buoy. This is because the Arctic sea ice advection is primarily regulated by two surface ocean circulation systems of the Beaufort Gyre (BG) and Transpolar Drift (TPD) (Kwok et al., 2013). Remote sensing sea ice motion (SIM) products can be used to simulate forward (backward) ice drift trajectories to track the destinations (origins) of ice floe (Lei et al., 2019) or estimate ice age by tracking the duration of ice drifting (Tschudi et al., 2020). Krumpen et al. (2019) analyzed the interannual variations in the advection patterns based on the reconstructed ice trajectories using a Lagrangian tracking approach, and investigated the impacts of ice advection patterns on ice mass or ice-associated material transmission in the TPD region. On this basis, Krumpen et al. (2020) estimated the original region of ice floe for the setup of the MOSAiC ice camp, in order to support interdisciplinary observations at the ice camp. In the practical process of establishing MOSAiC ice camp, the reconstructed ice drift trajectory using the SIM product is also an important basis for selecting the deployment location of ice camp. From the perspective of logistics, Granskog et al. (2016), Nicolaus et al. (2022), and Rabe et al. (2024) emphasized the impacts of dynamic deformation of ice floes on the safety of observation equipment deployed over the ice camps. However, there is still a lack of a comprehensive assessment of how deployment locations influence the subsequent drifting and destinations of ice camps and buoys at the basin scale in the Arctic Ocean.This study aims to address this gap by identifying the ideal deployment regions for ice camp or buoy using SIM products. The goal is to ensure uninterrupted observations while avoiding risks such as the drifting to the ice edge or to the exclusive economic zones (EEZs) of one country that is not involved in observation experiments within a shorter period than the expected duration.

During the Lagrangian observations, the atmospheric thermodynamic and dynamic forcing not only determine the seasonal evolution of sea ice itself, but also affect the heat and momentum exchanges between the atmosphere and sea ice. They can provide important backgrounds supporting the interdisciplinary studies based on Lagrangian observational data (e.g., Krumpen et al., 2021; Rinke et al., 2021). Under the background of Arctic amplification and sustained loss of Arctic

sea ice, understanding the climatological characteristics and long-term trends of atmospheric forcing and sea ice kinematics along the subsequent potential drifting trajectory is also essential for planning the deployments of ice camp or buoy. Moreover, it has gained widespread consensus, some atmospheric circulation patterns play a critical role in regulating Arctic sea ice advection. The Arctic Oscillation (AO) (Thompson and Wallace, 1998) regulates the axis alignment of the TPD and the extent of BG. At positive (negative) AO phases, the axis alignment of the TPD tends to shift westward (eastward) and the BG shrinks (expands) (Rigor et al., 2002). The wind anomalies induced by Dipole Anomaly (DA) (Wu et al., 2006) exhibit strong meridional forcing in the TPD region, with positive (negative) phases accelerating (decelerating) the sea ice drift along TPD (Wang et al., 2009). The Central Arctic air pressure-gradient Index (CAI), defined as the east-west gradient of sea level air pressure (SLP) across the central Arctic Ocean could regulate partly meridional wind forcing parallel to TPD (Vihma et al., 2012). The Beaufort High (BH) (Moore et al., 2018) is closely associated with sea ice circulation in the BG region (Proshutinsky and Johnson, 1997). These atmospheric circulation patterns affect sea ice drift trajectory and advection direction through various mechanisms and consequently affect the duration of Lagrangian observations relying on the ice floes. Thus, their regulatory mechanisms and seasonal variations needs further clarification regarding the evaluation of duration of the Lagrangian observations using Arctic ice floes.
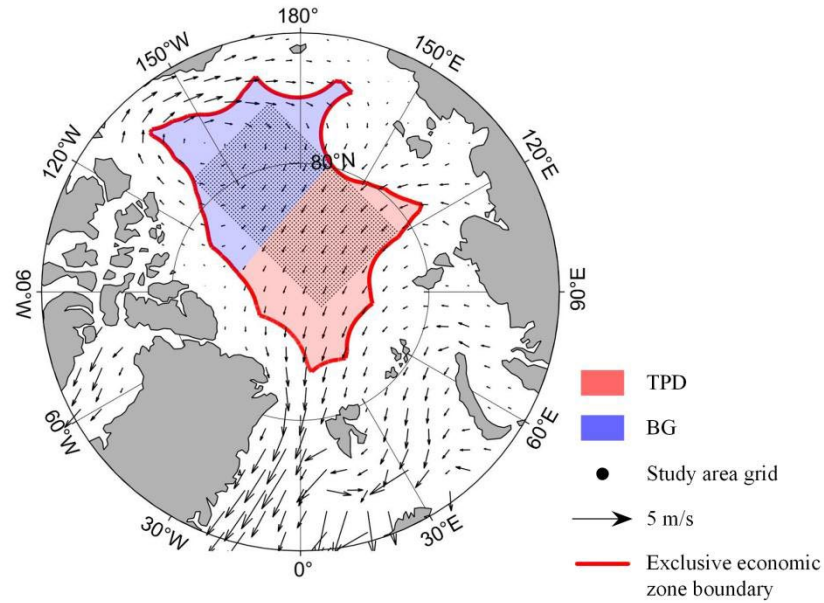
In this study, we organized the sections as follows. The datasets and methods used to reconstruct the sea ice drift trajectory and estimate the changes in atmospheric and ice conditions along the trajectory are briefly described in Sect. 2. The ideal deployment areas of Lagrangian observations, as well as changes in the atmospheric thermodynamic and dynamic forcing along the potential ice trajectories during each annual cycle from 1979–1980 to 2022–2023 (hereinafter referred to as 1979–2022) are presented in Sect. 3. The performance of the reconstructed method, the connection of the ice trajectories with the atmospheric circulation patterns, and the impact of EEZ boundary and deployment time on the sustainability of Lagrangian observations are discussed in Sect. 4. Conclusions are given in the last section. This study provides important cognitive foundation for the planning and implementation of Lagrangian observations relying on ice floes in the central Arctic Ocean.

2. Data and methods

2.1 Study area

Our study focuses on the reconstruction of sea ice drift trajectory in the central Arctic Ocean because it is difficult to maintain sufficient drifting observation time in the peripheral sea. Here, the central Arctic Ocean is defined as the high Arctic that excluded from the EEZs of any country, using the maritime boundary polylines (version 12) of the geodatabase provided

by the Flanders Marine Institute. To define the potential areas for identifying preferred deployment sites, we identified a rectangular area of 1.44×10^6 km^2, consisting of 2294 pixels on the 25-km polar stereographic grid, with area corners aligned with the EEZ boundary polylines, which covers approximately 53.5% of the central Arctic Ocean we defined (Fig. 1). The definition of such a rectangular area can effectively reduce computational cost relative to surveying the entire central Arctic Ocean. To demonstrate its rationality, we conducted surveys for the potential preferred area for ice camp or buoy deployment over the entire central Arctic Ocean using 1979–2023 climatology of SIM field. Results reveal that the effective starting points for deployment of ice camp or buoy with the subsequent drifting trajectory >= 9 months, avoiding drifting into the EEZ or beyond ice zone, occupy 91.6% of the defined rectangular area, which is higher than that (36.0%) for other regions within the central Arctic Ocean. Even during the most recent decade of 2013–2023, a period facing more severe and complex challenges due to thinner and younger ice, the rectangular area still contained 25.6% effective starting points, while other regions had none. Thus, in other regions within the central Arctic Ocean beyond our defined rectangular area, it is extremely difficult to identify suitable areas to deploy ice camps or buoys to maintain subsequent sufficiently long Lagrangian observations. Considering to save computational cost, we believe that definition of this rectangular area for reconstruction and analysis of sea ice drift trajectories in specific years is representative and reasonable. On the basic of the 1979–2023 climatology of Arctic SIM field, we also roughly defined boundaries to separate the BG and TPD regions, as shown in Fig. 1.

Figure 1. Study area. The black dots indicate grid points defined to identify the optimal area for the buoy or camp deployment. The arrows depict the mean SIM vectors from 1979 to 2023. The region delineated by the red lines represents the central Arctic Ocean, which is defined as the high Arctic that excluded the EEZs. The shaded blue and red areas roughly denote the Beaufort Gyre and Transport Drift regions within the central Arctic Ocean.

2.2 Data

a. Sea ice data

Due to the difficulty of obtaining long-time series, large-coverage SIM fields from high-resolution remote sensing images (e.g., Li et al., 2022; Fang et al., 2023), we used the 25-km Polar Pathfinder version 4.1 Sea Ice Motion Vectors from the U.S. National Snow and Ice Data Center (NSIDC; Tschudi et al., 2020), which is suitable for large-scale trend analysis, to reconstruct sea ice drift trajectories originating from the study area in 1979–2022. The Global Sea Ice Concentration Climate Data Records from the European Organization for the Exploitation of Meteorological Satellites Ocean and Sea Ice Satellite Application Facility (EUMETSAT OSI SAF; Lavergne et al., 2019) is utilized for evaluating ice conditions along the trajectory. This sea ice concentration (SIC) data is derived from the Scanning Multichannel Microwave Radiometer (SMMR), Special Sensor Microwave Imager (SSM/I), and Special Sensor Microwave Imager/Sounder (SSMIS) passive microwave satellite series sensors. The SIM and SIC data are projected onto the 25-km polar stereographic grid.

b. Buoy data

The trajectories of the buoys deployed over the Arctic ice were utilized to validate the reconstructed ice trajectories. To ensure the quality of validated SIM product, we constrained buoy selection to those situated 100 km offshore within the Arctic Ocean and excluded buoys south of the Fram Strait. The data of these buoys were derived from the International Arctic Buoy Programme (IABP), the SHEBA, the DAMOCLES (Brümmer et al., 2011), the German Arctic Research Expedition, and the Chinese National Arctic Research Expedition (CHINARE) during the summers of 2014, 2016, and 2018. The data collected by 32 buoys from 1997 to 2023, with 16 in each of the BG and TPD regions, were utilized for the validation of reconstructed ice trajectories in this study, with the details given in Table A1.

c. Atmospheric data

Atmospheric conditions were examined using atmospheric reanalysis data from the European Centre for Medium-Range Weather Forecasts Reanalysis v5 (ERA5; Hersbach et al., 2020). Hourly near-surface (2 m) air temperature, 10-m wind, snowfall, total precipitation and surface longwave radiation at about 30-km horizontal resolution are bilinearly interpolated to derive daily atmospheric conditions along the trajectories. ERA5 data is the next generation of the ERA-interim product. It has significant improvements in both temperature and wind fields in the Arctic Ocean (Graham et al., 2019b), and is able to reasonably characterize snowfall and precipitation (Wang et al., 2019), and the surface net longwave radiative flux under various weather conditions (Graham et al., 2019a).

162   Seasonal (autumn-OND, winter-JFM and spring-AMJ) indices of AO, DA, CAI, and BH were used to characterize the

163   regulatory mechanism of atmospheric circulation patterns on ice trajectories. The AO and DA indices were calculated from

164   the first and second empirical orthogonal functions of the SLP anomalies north of 70°N, utilizing monthly SLP from the

165   National Centre for Environmental Prediction/National Centre for Atmospheric Research to maintain consistency with

166   previous studies (Wu et al., 2006; Wang et al., 2009). Hourly SLP from ERA5 reanalysis was used to calculate the monthly

167   CAI (Vihma et al., 2012), defined as the difference between SLPs at 90°W, 84°N, and 90°E, 84°N. According to Moore et al.,

168   (2018), the ERA5 SLP anomaly over the region of 75°–85° N and 170°E–150°W were utilized to define the BH index,

169   which is more compatible with the BG from the perspective of sea ice circulation.

2.3 Methods

171   To assess the effective Lagrangian observation time, a survival time (ST) threshold for floes still drifting within the

172   Arctic ice region and avoiding entering EEZs is crucial. Based on a given ST threshold, regular grids (Fig. 1) were

173   established as the starting point for ice trajectory reconstruction to identify the preferred potential deployment areas of ice

174   buoy or camp. Reconstructed ice trajectories from these areas start on October 1, aligning with the approximate onset of ice

175   surface freezing season (Markus et al., 2009) and the setup time (October 3) of MOSAiC ice camp (Nicolaus et al., 2022).

176   According to Lei et al., (2019), the ice drift trajectories were reconstructed as follows:

177       $X(t) = X(t-1) + U(t-1) \cdot \delta_t,$ (2)

178   and $Y(t) = Y(t-1) + V(t-1) \cdot \delta_t,$ (3)

179   where X and Y are the zonal and meridional coordinates of ice trajectories, $U(t)$ and $V(t)$ are the ice motion components

180   at the time t along the ice trajectories, and the δ_t is the calculation time step of one day. The sea ice drift velocity field is

181   dynamically interpolated at each integration step using bilinear interpolation, which preserves instantaneous spatial

182   variations but may smooth out small-scale features due to the grid resolution of 25 km. For the NSIDC SIM product used in

183   this study, although there are errors in the individual motion estimates, these errors do not accumulate over long term

184   tracking because the motion estimates are largely unbiased (Tschudi et al., 2020). This is supported by the study of Tschudi

185   et al. (2010), who found a 27 km drift error over 293 days of tracking when compared to SHEBA buoy trajectories,

186   suggesting that errors can still be kept within limits over long term tracking. The validation of reconstructed trajectories with

187   buoy trajectories will be provided in Section 4.1.

188   When ice floes enter region with SIC < 15% or the EEZ of one country, the reconstructed ice trajectory is terminated,

189   and the time from October 1 to the terminal point is defined as the ST of ice floe, corresponding to the effective working

190 duration of an ice camp or a buoy that is deployed on it. Note that this study truncated reconstructed ice trajectories

191 exceeding one year (after 30 September of the following year) to focus on identifying areas unsuitable for deploying ice

192 camp or buoy where the ST of reconstructed trajectory did not meet the threshold.

193   Due to the fact that the SIM products were projected onto the 25-km polar stereographic grid, and the rectangular area

194 based on this grid was used as the starting point for ice trajectory reconstruction, the proportion of effective starting points

195 relative to the total grid points, corresponding to the a given threshold of ST, can be equivalent to the area ratio over the

196 study region. As shown in Fig. 2a, with a 10-month ST threshold, the available deployment areas in the central Arctic Ocean,

197 having the ST not less than 10 months with the probability >75% during 44 study years, are very limited (21.6% of the

198 rectangular study region), which is less than the 48.6% area when the ST threshold is set as 9 months. The probability with a

199 relative short duration less than 180 days was 1.9% for the effective region corresponding to the ST threshold of 6 months,

200 which was reduced to a negligible value of 0.8% (1.1%) for the 10-month (9-month, not shown) ST threshold; while that

201 with a relative long duration of 365 days or beyond was 70.9% for the ST threshold of 6 months, which increased to 82.6%

202 (77.8%) for the 10-month (9-month, not shown) ST threshold (Fig. 2b). Therefore, to ensure a broad range of deployment

203 areas, i.e., with a probability of > 50% across the entire study region, and ensure sufficient duration for Lagrangian

204 observations, we used a 9-month ST threshold for the subsequent analyses. It means the ST lasts until the end of June of

205 following year after the deployments, which is close the first drifting phase of MOSAiC ice camp (Nicolaus et al., 2022).

206 With this ST threshold, almost all the peripheral area of our defined rectangular region are identified as unsuitable for ice

207 camps and buoy deployment (Fig. 2a). This again proves that it is difficult to identify suitable sites for ice camp or buoy

208 deployments in other regions beyond our defined rectangular region in the central Arctic Ocean, and also confirms the

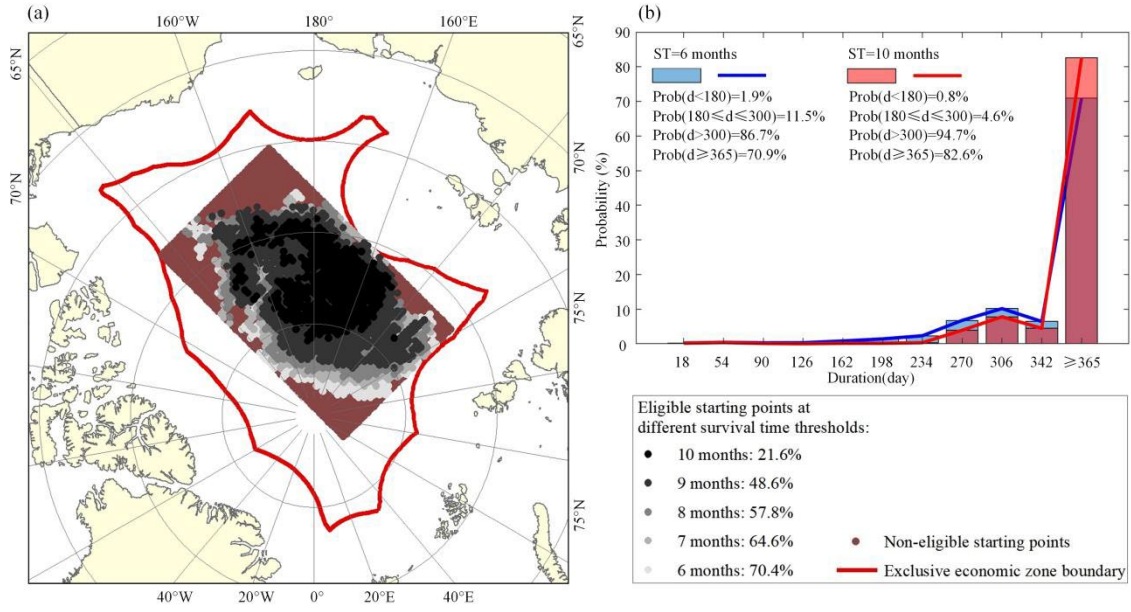209 rationality of our definition of this rectangular region.

210

Figure 2. (a) Spatial distribution of eligible starting points and (b) probability distribution of duration according to different thresholds of survival time in 1979–2022. Note that the truncation of reconstructed ice trajectory in this study is one year until 30 September next year. Thus, the proportions with the duration ≥365 days means the ice trajectory is still valid by 30 September of following year.

To verify the reliability of reconstructed ice trajectories, the Euclidean distance and cosine similarity against the buoy observations are used to quantify their distance and direction deviations. The Euclidean distance (D_f) is defined as follows:

$$D_f = \sqrt{\left(x_{buoy} - x_{cal}\right)^2 + \left(y_{buoy} - y_{cal}\right)^2} \ ,$$
(3)

where the subscripts of *buoy* and *cal* denote the coordinates of buoy trajectory and reconstructed ice trajectory, respectively. The metrics of distance deviation mainly include the Euclidean distance of the two trajectories at the endpoint, the average misalignment distance at the corresponding time and the root mean square error (RMSE). The Fréchet distance (Devogele et al., 2017) and cosine similarity are used to assess directional deviations in reconstructed trajectories. The Fréchet distance quantifies the trajectory similarity by comparing both spatial location and sequential placement of points, where smaller values indicate better reconstruction accuracy. Cosine similarity is an effective metric for assessing the geometrical similarity between the reconstructed trajectories and buoy trajectories (Gui et al., 2020), with a value approaching one denoting a high similarity between them. The cosine similarity (S_c) between the coordinate vectors of the reconstructed trajectory $(\overrightarrow{Q_{cal}})$ and buoy measurement $(\overrightarrow{Q_{buoy}})$ is calculated as follows:

$$S_c = \frac{\overrightarrow{Q_{cal}} \cdot \overrightarrow{Q_{buoy}}}{\left\|\overrightarrow{Q_{cal}}\right\|\left\|\overrightarrow{Q_{buoy}}\right\|} \ ,$$
(4)

where $\overrightarrow{Q_{cal}} = (x_{cal}(i), y_{cal}(i))(i = 1,2,3 \ldots \ldots)$ and $\overrightarrow{Q_{buoy}} = (x_{buoy}(i), y_{buoy}(i))(i = 1,2,3 \ldots \ldots)$.

To characterize regional differences between BG and TPD regions, we defined the starting points using the geometric

9

centers of grid points with a probability of reaching the BG or TPD region greater than 90% (BG: 80.04°N 157.71°W; TPD: 83.31°N 155.94°E) and that having ambiguous destination with a probability of reaching both regions between 40% and 60% (Both: 81.10°N, 177.89°E), and reconstructed the ice trajectory originating from these regions over 9 months for each cycle from 1979 to 2022 (Fig. 3). The atmospheric thermodynamic forcing, including the freezing degree days (FDDs) and thawing degree days (TDDs), snowfall, and precipitation, closely related to the ice thermodynamic growth and melting processes (Ricker et al., 2017a; Bigdeli et al., 2020), as well as the surface net longwave radiative flux, related to the feedbacks of clouds and sea ice itself on the near-surface atmosphere (Graham et al., 2017), were estimated along the reconstructed ice trajectories. FDD (TDD) refers to the integral of daily average near-surface air temperatures below −1.8°C (above 0°C) over the study period, derived from ERA5 hourly air temperatures, with a negligible bias (7.18 $\times 10^{-7}$ K) compared to the daily air temperatures obtained directly from ERA5. The dynamic response of sea ice to atmospheric forcing is characterized using the ice-wind speed ratio (e.g., Herman and Glowacki, 2012).
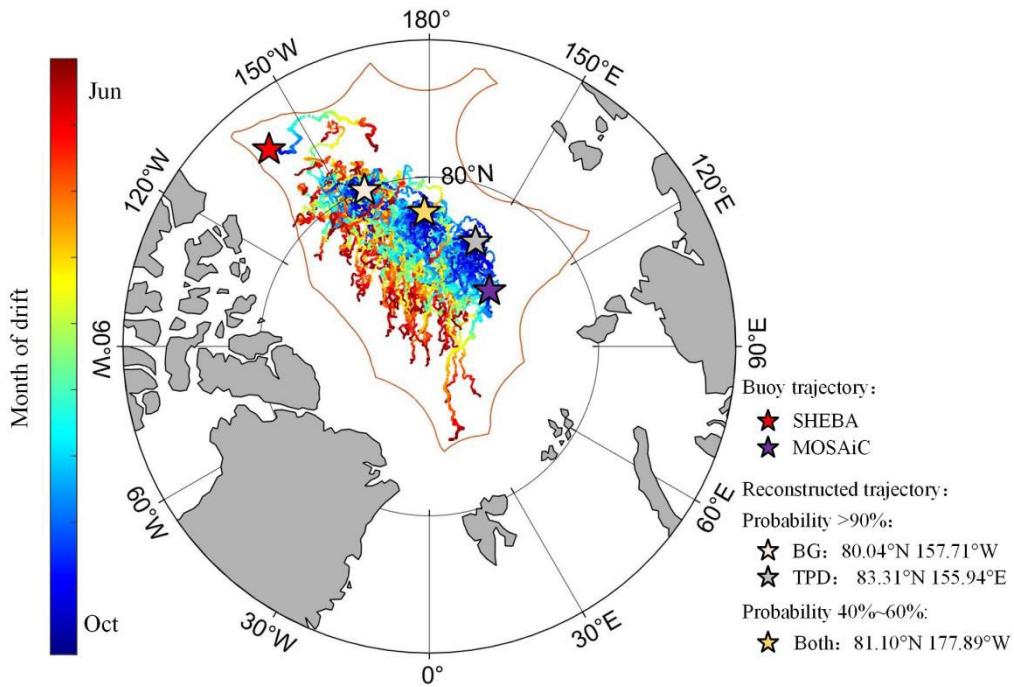
Figure 3. Reconstructed 9-month sea ice trajectories in 1979–2022, starting from three geometric centers of grid points with a probability of reaching the BG or TPD region greater than 90% and that having ambiguous destination with a probability of reaching both regions between 40% and 60%. For comparison, the partial drifting trajectories of SHEBA and MOSAiC ice camps started from October 3 of 1997 and 2019 to the time of 9 months after deployment are also shown.

245 **3. Results**

246 **3.1 Spatial distribution of the effective starting points of reconstructed ice trajectories with 9-month ST**

247   Using the reconstructed ice trajectories for each ice season from 1979 to 2022, the influence of the specific starting

248 point on the ST and its destination is assessed here. The results reveal that the effective probabilities (the ratio between the

249 effective years to all study years from 1979 to 2022) of starting points with the reconstructed ice trajectories having

250 sufficient ST of no less than 9 months ranged from 9.1% to 90.9%. Drifting from the region close to north of the East

251 Siberian and Laptev seas (centered at about 82°N and 160°E), the probability over the 44 years is relatively high than other

252 regions, generally exceeding 75%. The likelihood of sea ice drifting into the EEZs or beyond the ice zone increased when the

253 starting point approached the corners of rectangular study region, particularly in the downstream region of the TPD, where

254 the probability is notably less than 20.0%. The eligible points shown in Fig. 4b indicated that the locations (with a size of

255 $7.0 \times 10^5 \, \mathrm{km^2}$) as the starting point of reconstructed trajectories with the ST >= 9 months within 33 years (or 75%) or beyond

256 from 1979 to 2022. Among them, the blue dots represent moderate-recommendation zones in the central Arctic Ocean for ice

257 camp or buoy deployment, where Lagrangian observations have a 75–85% probability of lasting sufficiently long, with these

258 zones occupying 80.4% of the eligible area. The red dots, on the other hand, having a probability of > 85%, are

259 high-recommendation zones, occupying 19.6% of the eligible area.

260   The probabilities of termination of reconstructed ice trajectory reaching the BG or TPD region during the study period

261 are illustrated in Fig. 4c–d. From 1979 to 2022, as expected, the ice floes that tend to drift to the BG region (Fig. 4c) are

262 mainly originating from the southwest part of the defined rectangular area; while the ice floes that tend to drift to the TPD

263 region (Fig. 4d) are mainly originating from the northeast part of the rectangular area. However, there is also a large

264 overlapping area between these two regions, and the magnitude of the probabilities exhibits a regular regional variability

265 pattern for the specific regions. This suggests that the location of the starting point has a crucial influence on the subsequent

266 ice advection. Thus, the deployment areas of the ice camp or buoy would determine their drift trajectory and final destination

267 to a high degree. The number of eligible starting points, whose reconstructed trajectory reached the TPD region with ST of

268 no less than 9 months, accumulated over 75% years of the 44-year study period, was 2.2 times that of such starting points

269 that reached the BG region. This indicates that sea ice originating from eligible starting points is more likely to reach the

270 TPD region. For the ice floes originating from the junction zone between the BG and TPD regions (yellow strip in Fig. 4b),

271 defined using the climatological SIM field, the probability of reconstructed ice trajectories reaching these two regions ranges

272 from 42.5% to 52.5%, without obvious regional tendency for ice advection destination.

273   Noting the symbolic shift in the physical nature of Arctic sea ice after 2007 (Sumata et al., 2023), we further calculated

the probability distribution of the starting point with the termination of the reconstructed ice trajectory reaching the BG or TPD region for the sub periods prior to and after 2007, as shown in Fig. 5. The probabilities of starting points having the sufficient ST of no less than 9 months ranged between 14.3% and 92.9% in 1979–2006, which changed to 7.3%–87.5% since then, indicating a greater variability after 2007 (Fig. 5a–b). The size of ideal deployment area (red and blue dots), with a probability > 75% in Fig. 5c–d, was reduced obviously in 2007–2022 (2.1×10^5 km^2) by 81.3% compared to that derived from 1979–2006 (11.2×10^5 km^2). In particular, the area of high-recommendation zones (red dots) has shrunk from 6.9×10^5 km^2 in 1979–2006 to an almost negligible area of 1.1×10^4 km^2 in 2007–2022. Such a conspicuous reduce in the moderate- and high- recommendation zones suggests that the deployments of ice camp or buoy, with an intention to obtain sufficiently long Lagrangian drift observations, in the central Arctic Ocean become more challenging as sea ice decreases.

The spatial distributions of the probabilities of reaching the BG and TPD regions in two sub periods prior to or after 2007 are similar to those derived from the whole study period (Fig. 5e–h); and the spatial proportions of starting points with > 75% probability of reaching the two regions varied slightly for two sub periods, with changes ranging from 0.7% to 4.8% relative to the full period. This suggests the destination of ice floe advection is relatively stable, which is mainly associated with the Arctic sea ice circulation patterns (detailed analysis will be provided in Section 4.2).
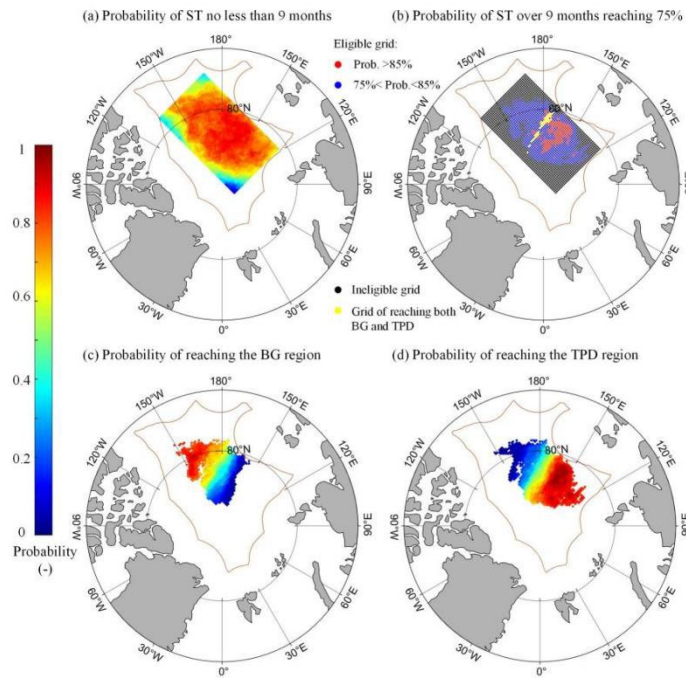

Figure 4. Spatial distribution of probability that sea ice drifting from a defined grid point satisfies the following conditions in 1979–2022: (a) the ST within the central Arctic Ocean for no less than 9 months; (b) the region with the probability of ST over 9 months reaching 75% (red and blue dot), also shown is the junction zone between the BG and TPD regions (yellow strip), defined using the climatological SIM field; and the probabilities with the destinations of reconstructed trajectories reaching the (c) BG or (d) TPD region.
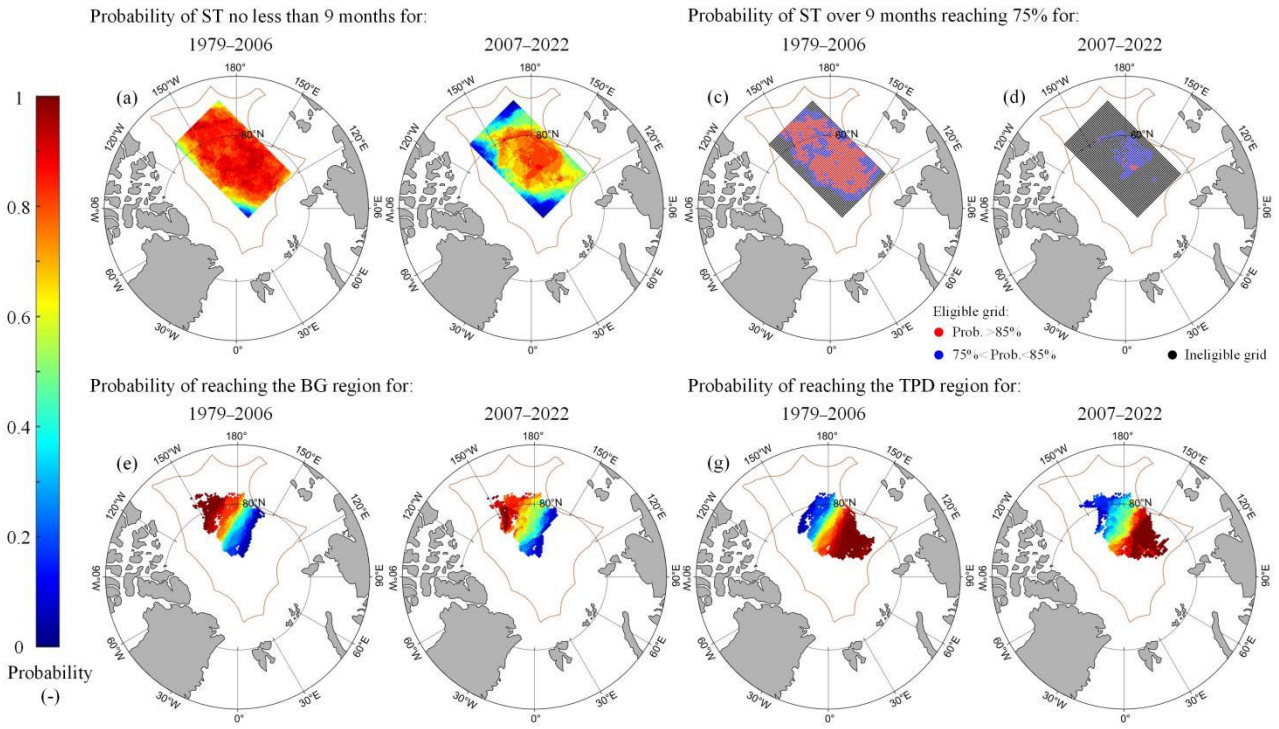
Figure 5. Spatial distribution of probability that sea ice drifting from a defined grid point in two sub periods of 1979–2006 and 2007–2022 under the following conditions: (a–b) probability of ST of no less than 9 months; (c–d) the region with the probability of ST over 9 months reaching 75% (red and blue dot); and probability of reaching the (e–f) BG or (g–h) TPD region.

3.2 Changes in atmospheric thermodynamic and dynamic forcing along the trajectories

Sea ice thermodynamic growth is regulated by both atmospheric and oceanic forcing. Since the oceanic heat flux underneath the ice is relatively weak during the freezing season (Lei et al., 2022), near-surface air temperature could be considered as the most decisive parameter regulating ice growth and is a major atmospheric forcing factor for the sea ice growth analysis model (Leppäranta, 1993). In 1979–2022, the average air temperature along ice trajectories was higher in the TPD region (-17.6 °C) than in the BG region (-18.2 °C), with a slightly higher increasing trend (0.096 °C/yr) than that in the BG region(0.082 °C/yr). This is consistent with enhanced warming in the Atlantic sector of Arctic Ocean (Rantanen et al., 2022). Despite significant increases in air temperatures in both regions, the occurrence of extremely high air temperatures exceeding 90th percentile of daily mean from 1979 to 2022, also defined as hot days by Vautard et al., (2013), did not change significantly and occurred mainly in June, with similar frequencies in both regions (BG: 7.3%–12.4%, TPD: 6.6%–13.2%). This implies that extremely events with high near-surface air temperature are largely concentrated in the initial stage of ice melting (Markus et al., 2009). These events are often accompanied by the process of rainfall (e.g., Robinson et al., 2021). The average precipitation along the trajectories increased significantly in both regions (BG: 0.13 mm, TPD: 0.10 mm, $P < 0.05$) from 1979 to 2022, but a significant increase in accumulated snowfall was only observed in the BG region (0.50 mm water equivalent/yr, $P < 0.05$). The TPD region is more susceptible to a shift in precipitation form snowfall to rainfall due to

312 warmer conditions (Cohen et al., 2020), resulting in an insignificant change in snowfall. Especially in late spring and

313 summer, the increased precipitation in the form of rain would accelerate the melting of the sea ice surface, promote melt

314 ponds formation (e.g., Feng et al., 2021), and trigger positive albedo feedbacks (e.g., Goosse et al., 2018).

315 To further investigate the potential impact of near-surface temperature on sea ice melting or freezing, we also calculated

316 FDD and TDD along the trajectories in 1979–2022. The BG region had higher FDD than the TPD region, indicating warmer

317 conditions during the freezing season in the TPD region despite its higher latitude (Fig. 6). FDD in the BG region showed a

318 significant decreasing trend ($P<0.05$), slightly larger than that in the TPD region. However, the magnitude of TDD along the

319 trajectories reaching both regions of BG and TPD did not differ considerably and did not reveal a clear trend due to the

320 insignificant warming trend for the summer in the Arctic Ocean. In winter, the average surface net longwave radiative flux

321 along the trajectory in the TPD region was upward, indicating the heat loss from the sea ice-ocean system to the low

322 atmosphere, with the peak of probability distribution in its absolute value decreasing from about 57.5 W/m^2 prior to 2007 to

323 about 52.5 W/m^2 after 2007. However, such shift in the BG region was relatively weak from about 52.5 W/m^2 to about 50.0

324 W/m^2 (Fig. 7). This indicates that the weakened radiational cooling effect from the surface in the TPD region under the

325 clear-sky conditions was more pronounced compared to that in the BG region, which also can be attributed the difference in

326 the winter warming trend between two regions. Moreover, the frequency with the net longwave radiation feature under the

327 opaquely cloudy state during the winter, having the typical value of > -10 W/m^2 (Graham et al., 2017), increased from 3.6%

328 in 1979–2006 to 4.3% in 2007–2022 in the TPD region, while it decreased from 4.3% to 4.2% in the BG region. This is

329 likely due to enhanced cyclonic activity in the Atlantic sector of Arctic Ocean (e.g., Zhang et al., 2023).
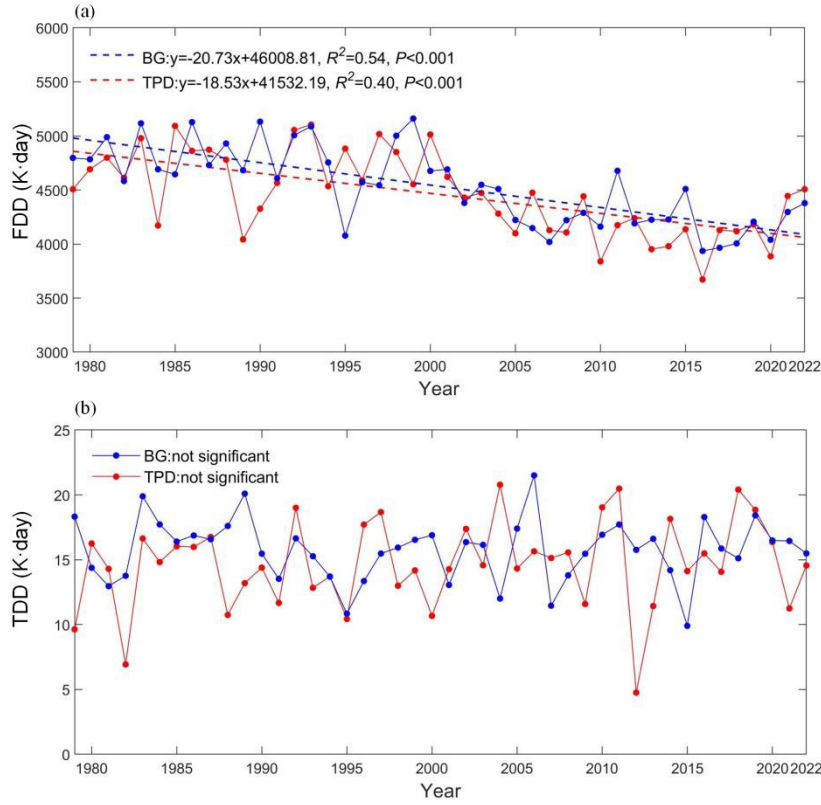
Figure 6. Changes in (a) FDD and (b) TDD during October to June in two regions from 1979 to 2022.
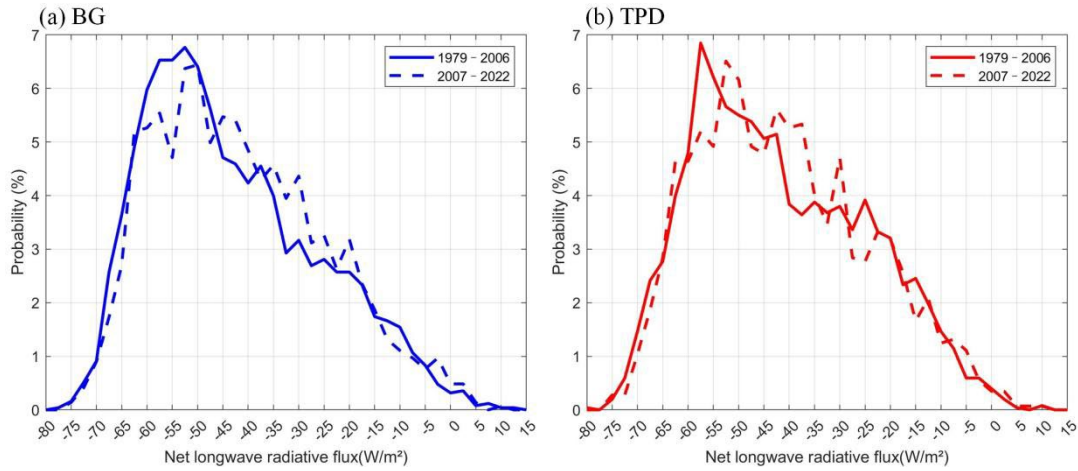

Figure 7. Probability distribution of winter surface net longwave radiative flux along the trajectories in the BG and TPD regions for two
sub periods of 1979–2006 and 2007–2022, with negative values denoting the upward flux from the surface.

The dynamic response of sea ice to wind forcing can be characterized using the ice-wind speed ratio (Herman and
Glowacki, 2012). The seasonal average ice-wind speed ratio along the ice trajectories was largest in autumn (TPD: 1.55%,
BG: 1.52%), which may be due to the relatively weak sea ice consolidation at that time (e.g., Lund-Hansen et al., 2020).
Note that, the ice-wind speed ratio was slightly lower than those obtained from buoy observations close to the North Pole by
Haller et al., (2014), as the remote sensing SIM product typically underestimates SIM speeds due to the low temporal
resolution (Gui et al., 2020). This ratio is also overall lower than the typical values in free-drift analytical solution

1

(Leppäranta, 2011), likely because higher SIC increases internal ice stress, enhancing resistance against SIM and reducing sea ice response to wind forcing. Since 2007, the seasonal average ice-wind speed ratio in the BG region increased to 1.6±0.3% for autumn, winter and spring seasons, overwhelming the TPD region by about 10.0%. This indicates an ongoing enhancement of dynamic response of sea ice to wind forcing in the BG region, linked to the replacement of thick multi-year ice by thin seasonal ice (Babb et al., 2023). Therefore, the SHEBA campaign data (e.g., Lindsay, 2002) are no longer representative of the current ice state in the BG region.

4. Discussions

4.1 Assessment of reconstructed sea ice drift trajectories

To validate the reliability of the ice trajectory reconstruction method using remote sensing SIM product, we used data from 16 buoys in each of the BG and TPD regions (Table A1). Within the initial 100 days, most misalignment distances were less than 50 km (Fig. 8a), with RMSEs of 50.9 km. However, the reconstructed trajectories from the deployment sites of 5 buoys were misaligned with the buoys trajectories by a relatively large distance (146.3–173.0 km after 100 days), likely due to the complex wind conditions at the early drifting stage of these buoys. These buoys experienced relatively high wind speeds (6.8±2.7 m/s) in the first 10 days, with over 60.0% of days exceeding 6.0 m/s, which is higher than the climatological average since 1979 (5.6±0.4 m/s). Conversely, the distribution of initial 10-day wind speeds in our reconstructed trajectories in the BG and TPD regions over the 44-year period is mainly concentrated in the range up to 6.0 m/s (>58.0%), with modal wind speeds ranging from 4 to 5 m/s (Fig. A1). This indicates that most reconstructed trajectories in this study did not experience such strong wind conditions that affect the accuracy.

Excluding the 5 buoys with complex initial wind conditions, the average misalignment distances between the reconstructed trajectories and the buoy trajectories (10 cases) after 9 months are 59.0±41.4 km (about 2.5 pixels of ice motion product), and the RMSE is 68.6 km. The mean Fréchet distance was 89.6 km, the cosine similarities all above 0.92, and the average endpoint Euclidean distances is 114.4±87.5 km. This high geometric similarity ensures appropriate advection direction and destination of the reconstructed trajectories. Regionally, there is a better reconstruction performance in the BG region than that in the TPD region. After 9 months, the average misalignment distance in the BG region (3 cases) is about 23.0 km, which is 30.9% of that in the TPD region (7 cases), and the Fréchet distance is about 55.5 km, which is 48.1% of that in the TPD region, consistent with the visual comparison of drift trajectories shown in Fig. 8b. This may be due to the larger SIM speed and its meridional gradient in the TPD region, especially in the southern region. All reconstructed trajectories in the TPD region terminate at a further northward location compared to the corresponding buoy

369 trajectories. This leads to a relatively adventurous estimate of the effective duration of ice trajectories in the TPD region.

370 However, we estimate this uncertainty to be approximately 1.6% (or 4.3 days) compared with the buoy measurement, which

371 looks trivial.

372 In addition, the semi-Lagrangian method also has been proposed by combining the Lagrangian and Eulerian aspects to

373 reconstruct ice trajectories through a time-stepping procedure (Sagawa and Yamaguchi, 2006). Therefore, we also compared

374 the reconstructed trajectories obtained using the Lagrangian or semi-Lagrangian methods. For two starting points with > 90%

375 probability of reaching the BG and TPD regions, the reconstructed trajectories of the two methods showed high similarity,

376 with Fréchet distances of 8.3 km, average cosine similarity of above 0.99 and average misalignment distances of 3.5±1.6 km

377 in the BG region and 2.5±1.2 km in the TPD region, respectively. However, relative to the validation data measured by 30

378 buoys, the semi-Lagrangian method exhibited larger errors compared to the Lagrangian method used in this study. The

379 endpoint distances between the trajectories reconstructed using the semi-Lagrangian method and the buoy trajectories after 9

380 months (10 cases) were 118.6±88.2 km, with the misalignment distances of 61.1±40.9 km, RMSEs of 70.8 km, Fréchet

381 distances of 90.1 km, and cosine similarities all above 0.92. These statistical matrices are larger than those obtained by the

382 Lagrangian method by 3.67%, 3.56%, 3.21%, and 0.56%, with comparable cosine similarities, respectively. It is likely is

383 because the semi-Lagrangian method does not directly track individual particles as precisely as the Lagrangian method

384 (Subich et al., 2020), affecting its accuracy in reconstructing ice trajectories.

385 To further assess the reliability and the stability of the ice paths, we also conducted a closed-loop examination by

386 reconstructing backward ice drift trajectories from endpoints of the original forward-reconstructed trajectories. This

387 verification test required reconstruction of backward trajectories to return to their starting points after the same time period.

388 Specifically, we initiated backward reconstructions from hotspot regions, i.e., the region where sea ice is more likely to reach

389 and retain (defined by a density-based clustering method with 75% probability of ST >9 months during 1979–2022) at the

390 endpoints of forward trajectories. Consequently, 66.3% of backward trajectories are projected to return to recommended

391 regions, with 49.2% and 17.1% reaching the moderate- and high- recommendation zones, respectively (Fig. 9). This suggests

392 that the recommendation zones, as a source area for sea ice, have stable paths. This closed calibration testing also

393 demonstrates the high confidence in the reconstruction method of ice trajectory.

394 To test the robustness of the duration, we estimated the impact of year, starting position and interpolation method on the

395 duration, using the starting points reaching the BG or TPD region over 90% as an example. The results showed that the

396 standard deviation of duration in 1979–2022 amounted to 76.0 days, this standard deviation decreases to 20.7 days in 2007–

397 2022, which corresponds to 7.2% of the mean duration. It should be noted that this study mainly focuses on the mean

398 duration characteristics at the climate scale. The difference between the mean duration in case of starting position offset (±10

399 km) and the results obtained for the starting position accounts for about 1.1%, and the mean duration obtained from the ice

400 trajectories reconstructed with the nearest neighbor interpolation differs from the results obtained with the bilinear

401 interpolation by an average of 7.6%, which proves that small changes in the initial coordinates and the interpolation method

402 barely affect the reliability of the duration.
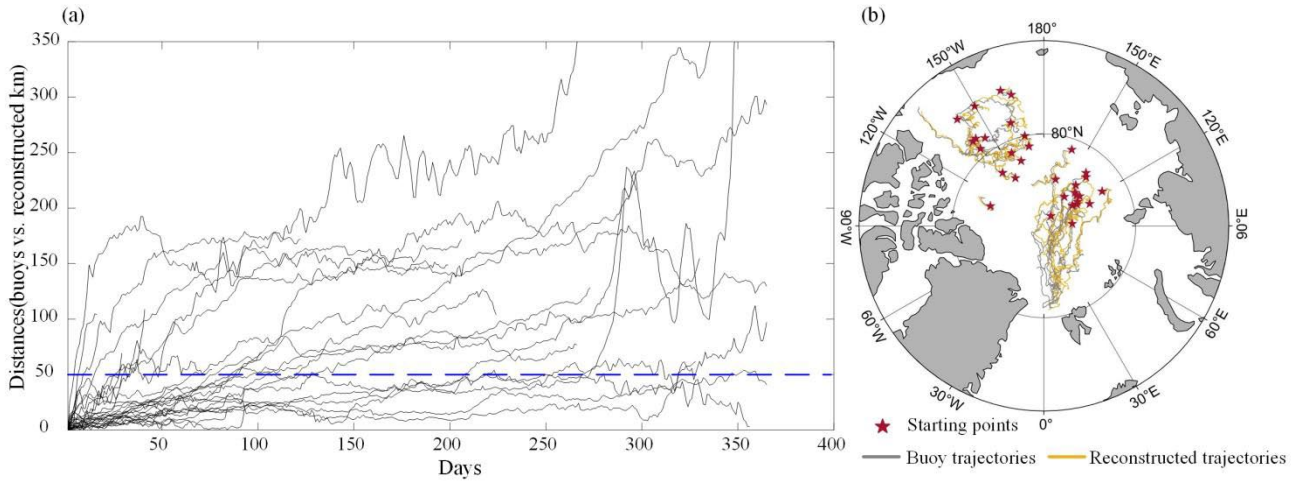
403

404 **Figure 8.** Comparison of reconstructed ice trajectories with buoy trajectories: (a) misalignment distances over time for trajectory pairs; (b)

405 trajectory pairs from the deployment site of buoys.
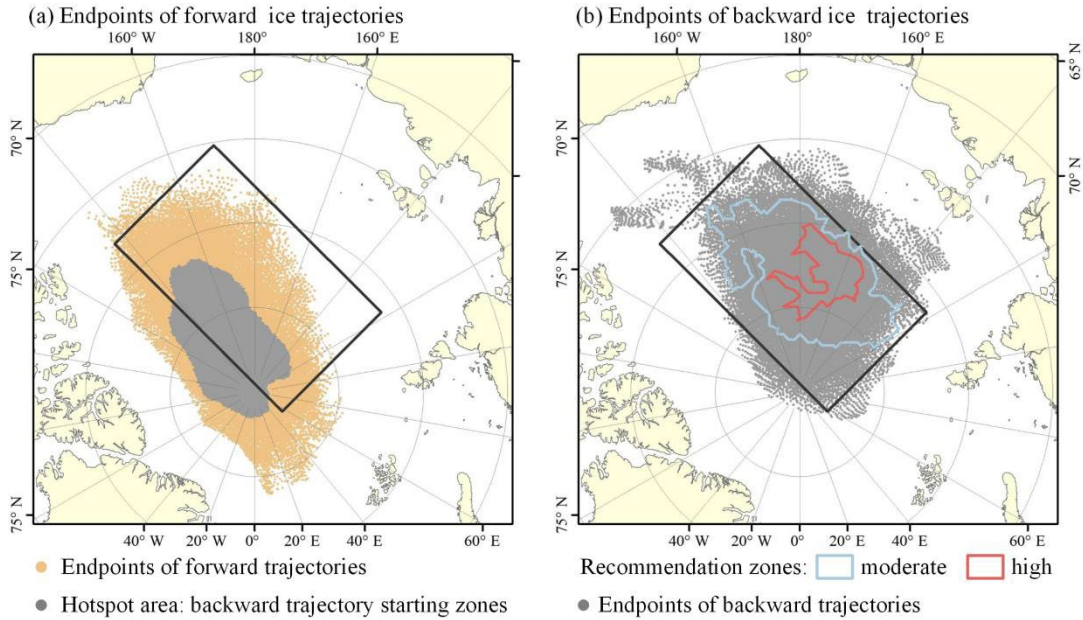
406

407 **Figure 9.** Spatial distribution of endpoints of forward- and backward- reconstructed trajectories: (a) forward trajectory endpoints and

408 hotspot regions; (b) endpoints of backward-reconstructed trajectories from hotspot regions.

409 **4.2 Links of endpoints of ice trajectories to atmospheric circulation patterns**

410 Based on three scenarios for ice trajectory endpoints, i.e., > 90% probability of reaching the BG or TPD region and 40–

1

60% probability of reaching both regions, we explored the links of endpoints of ice trajectories to atmospheric circulation patterns (Table 1). We also analyzed the statistical relationship (Table 2) between the distance from the endpoint to Fram Strait (80°N) for the ice trajectories reaching the TPD region and atmospheric circulation indices, which allows exploring the potential impact mechanisms of atmospheric circulation patterns on the sea ice outflow from the central Arctic Ocean.

For ice trajectories reaching the TPD region, autumn CAI, DA showed stronger correlations with endpoint latitude after 9 month (R^2: 21.8% and 32.5%, $P<0.05$) and with the distance between the endpoint of the ice trajectory after 9 months and the Fram Strait (R^2: 21.8% and 32.5%, $P<0.05$) than BH. This is due to the fact that these indices directly modulate meridional wind forcing, i.e., their positive phases enhance transpolar drift by intensifying southerly winds across the TPD region (Wu et al., 2006; Vihma et al., 2012). In contrast, BH primarily affects longitude of ice trajectory through zonal adjustments of the TPD pathway. When the BH index is positive, the BG squeezes the axis alignment of the TPD eastward, lengthening the distance that ice advects along the TPD toward the Fram Strait. This mechanistic difference explains why in the TPD region CAI is associated with latitudinal changes in the ice drift trajectory, while BH affects its longitudinal changes. Therefore, it is necessary to take the autumn CAI and DA index into consideration for predicting the subsequent trajectory of ice floe, as well as the buoy or camp deployed on it in the TPD region.

For the ice trajectory reaching the BG region, although sea ice circulation in the BG region is driven by anticyclonic wind stress curl associated with the positive BH index (Proshutinsky et al., 2002), the BH did not reveal more effective interpretability for the location of the ice drift endpoints in this region than other indices. This may be because the influence of BH on the ice advection in this region is susceptible to interference from the impacts by other atmospheric circulation patterns, in particular, the DA and the associated meridional wind anomalies (e.g., Wang et al., 2009). The weaker latitude than longitude correlations (R^2: 9.5% and 19.1%, $P<0.05$) between the autumn CAI and DA and the endpoint after 9 months reflect the fact that the BG can suppress meridional transport because sea ice motion in the BG region is mainly driven by anticyclonic circulation. Moreover, for sea ice that has the potential to reach both regions of BG and TPD, all atmospheric circulation indices in autumn also had a significant explanatory level for the latitude of endpoint and its distance to the Fram Strait after 9 months ($P<0.05$).

Since atmospheric circulation patterns during the start stage of ice drift in autumn, especially for the CAI and DA, had a strong influence on the endpoints of ice trajectories after 9 months in both regions of BG and TPD, we further analyzed scenarios where these indices exhibit extreme positive (negative) anomalies, defined with the value higher (lower) than the 1979–2022 climatology by one standard deviation (Fig. 10). When CAI and DA are at extreme positive (negative) phases, the spatial proportions of starting points with a 9-month ST threshold for more than 75% years are 75.2% (46.3%) and 86.0%

(44.1%), respectively, which are greater (less) than the spatial proportions obtained from the mean field in 1979–2022 (48.6% as shown in Fig. 2). This suggests that the extreme scenarios of autumn CAI and DA have a pronounced modulating effect on the ideal deployment areas for Lagrangian observations, with a wider range of ideal areas at their extreme positive phases. Under extremely positive phases of CAI and DA, the preferred area of deployment tends to extend to the Chukchi Sea and the Canada Basin, while at the negative phase it prefers the northern Laptev Sea. However, the extremely positive phase of the autumn CAI only favors a trivial increase (by 2.2%) in the spatial proportion of points with > 75% probability of reaching the TPD region compared to the average state over 44 years. The extreme negative phase of the autumn DA, on the other hand, significantly increases the probability of reaching the BG region, and the spatial proportion > 75% is 1.5 times that obtained from the whole study period.

Table 1. Coefficient of determination (R^2) between atmospheric circulation indices and location (longitude/latitude) of sea ice trajectory endpoint after 9 months in 1979–2022.

	Regional tendency	Autumn CAI	Autumn AO	Autumn DA	Autumn BH
Longitude of endpoint	TPD	n.s.	n.s.	n.s.	n.s.
	BG	*0.218*	*0.181*	n.s.	0.149
	TPD/BG	*0.215*	*0.158*	n.s.	0.145
Latitude of endpoint	TPD	*0.225*	n.s.	**0.261**	*0.216*
	BG	0.095	n.s.	*0.191*	n.s.
	TPD/BG	**0.255**	0.092	**0.333**	*0.210*

Note: Significance levels are $P < 0.001$ (bold), $P < 0.01$ (italic) and $P < 0.05$ (plain); n.s. denotes insignificant at the 0.05 level.

Table 2. Coefficient of determination (R^2) of autumn atmospheric circulation indices for the distance from the sea ice trajectory endpoint after 9 months to the Fram Strait in 1979–2022.

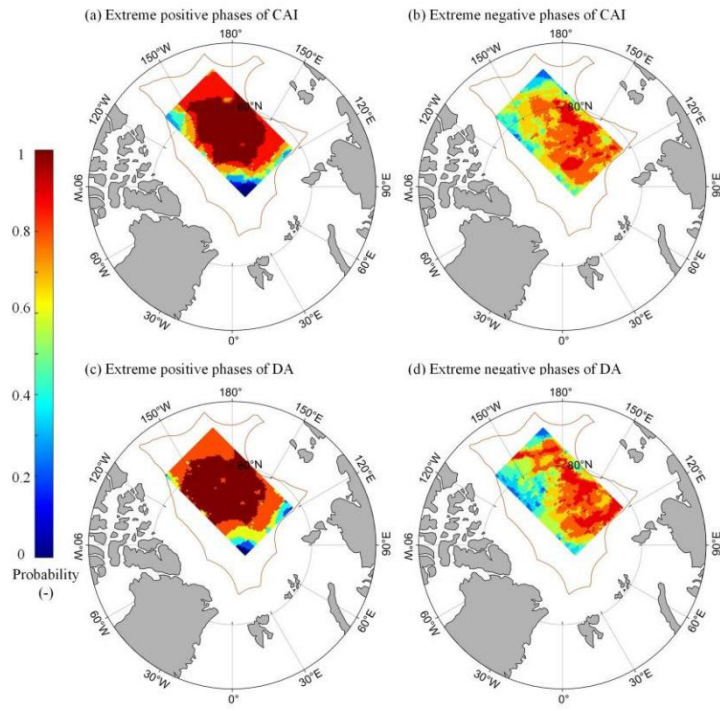| Regional tendency	Autumn CAI	Autumn AO	Autumn DA	Autumn BH
TPD	**0.309**	n.s.	**0.325**	*0.218*
TPD/BG	**0.303**	0.128	**0.239**	**0.247**

Note: Consistent with Table 1.

Figure 10. Spatial distribution of the probability that the ST of sea ice drifting from a defined grid point is no less than 9 months at the extreme positive and negative phases of the autumn CAI and DA for 1979–2022.

4.3 Impact of the EEZ boundary and deployment time on the ST of ice trajectory

The ST of reconstructed ice drift trajectories, or the potential Lagrangian observations on the basis of ice camp and buoy is limited to a high extent by the EEZ boundary. To quantitatively evaluate the impact in this regard, we hypothesized a desirability of enhanced international cooperation to reduce the impact of geopolitical boundaries on this type of observations, and identified the ideal deployment areas for Lagrangian observations under this scenario. It is found that the probability of ST exceeding 9 months for ice trajectories reconstructed from all grids in the rectangular study region ranged from 45.5% to 90.9% between 1979 and 2022 without the limitation of the EEZ boundary. The spatial range with probabilities > 75% (i.e., 33 years) for the ST threshold of 9 months extends to 83.7% of the whole rectangular study region, much larger compared to that (48.6%) with the limitation of the EEZ boundary. Disregarding the EEZ boundary, the increase in eligible starting points with > 75% probability is proportional to the used ST threshold (Table 3). Especially for the 10-month ST threshold, the eligible area increases by over 150% compared to that with the limitation of the EEZ boundary. Disregarding the EEZ boundary, the increase in eligible starting points in the rectangular study region with > 75% probability of reaching the BG or TPD regions is also proportional to the ST threshold. Particularly for the 10-month ST, the number of eligible starting points reaching the BG or TPD region increases by over 100% through removing the limitation of EEZ boundary. For starting points with a close probability of reaching both regions of BG and TPD, the spatial proportion of eligible starting points would instead be suppressed compared to that estimated with the consideration of the EEZ boundary.

2

This is because these eligible starting points are primarily located at the junction of two regions of BG and TPD and relatively far from the EEZ boundary.

For the period 1979–2022, the average Lagrangian observation duration in the rectangular study region disregarding the EEZ boundary is about 298.0±25.7 days, which extends by about 34.3 days compared to those estimated with the consideration of the EEZ boundary. Regionally, the Lagrangian observations located in the BG and TPD regions would be further extended by about 20.5 days (286.1±128.1 days) and 5.0 days (298.3±114.4 days), respectively. This suggests that the EEZ boundary has a slightly larger impact on the observation duration in the BG region compared to the TPD region, because the EEZ boundary in the downstream of TPD is overall close to the marginal ice zone. Spatially, for sea ice reaching the BG region, the added eligible starting points are located in the southern part of the BG, as shown in Fig. 11. Sea ice originating from these locations might be more strongly affected by the clockwise ice circulation of the BG and cross beyond the EEZ boundary in the south more easily. For the ice trajectories reaching the TPD region, the added eligible starting points are located in the south of the study region or in the sector facing the Fram Strait. Sea ice originating from these areas might have been advected more rapidly to cross the EEZ boundary in the Atlantic sector.

Table 3. Increased spatial percentage in eligible starting points without considering the EEZ constraints compared to those estimated with the constraints.

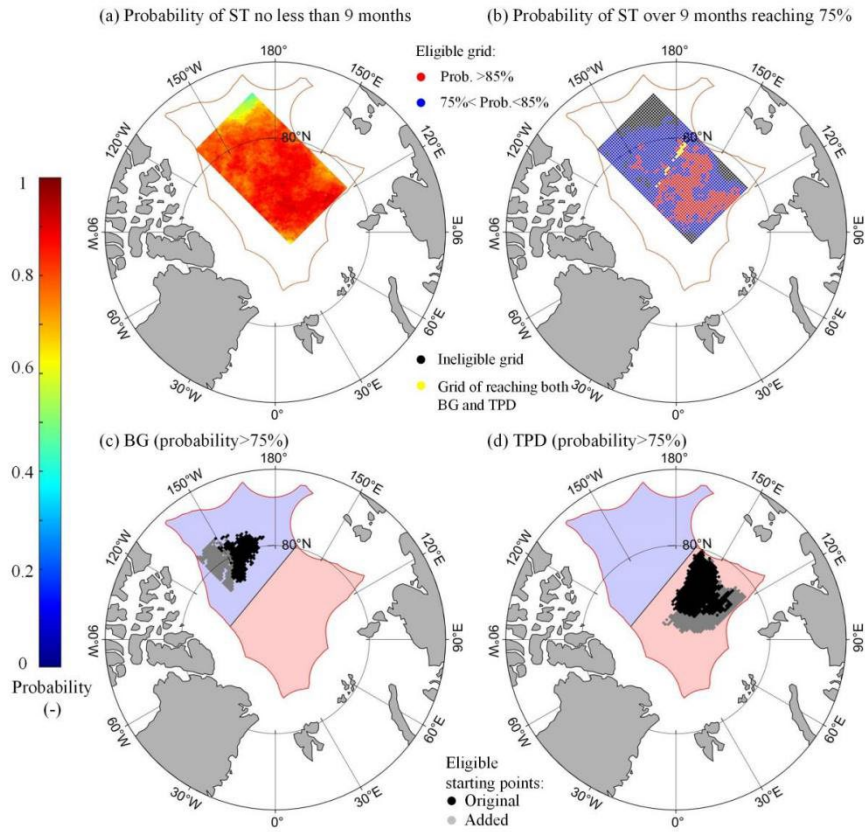| ST threshold in the ice zone (months)	6	7	8	9	10
Case 1: probability of ST over corresponding ST > 75%	21.5%	32.0%	46.3%	72.0%	157.3%
Case 2: probability of reaching the BG region > 75%	10.8%	17.2%	21.5%	72.4%	111.1%
Case 3: probability of reaching the TPD region > 75%	3.1%	11.5%	21.2%	49.0%	144.0%
Case 4: probability of reaching the BG or TPD region ranging between 40% and 60%	–35.4%	–44.1%	–47.7%	–54.5%	–72.7%

2

Figure 11. Assuming that the EEZ boundary constraints are not considered in 1979–2022: (a) spatial distribution of the probability of ST in the ice region no less than 9 months; (b) the region with the probability of ST over 9 months reaching 75% (red and blue dot), also shown is the junction zone between the BG and TPD regions (yellow strip); and (c–d) the added eligible starting point (gray) with > 75% probability of reaching the BG or TPD region, compared to those estimated with the EEZ constraints (black).

To further assess the influence of setup time of ice camp or buoy on the potential duration of subsequent observations, using the starting points reaching the BG or TPD region over 90% (Fig. 3), we calculated the duration with the deployment date ranging from August 15 to November 1 (Fig. 12). The mean duration of Lagrangian observation in the two regions decreases gradually from 296.1±11.8 days for the deployment on August 15 to 279.9±17.1 days according to the deployment on November 1. Although the advanced deployment of ice camp or buoy based on ice floes to August 15 may result in longer observation time, approximately by 10.0 days, compared that derived from the deployment on October 1. We still argue that it is more appropriate to implement the deployments of ice camp or buoy over the Arctic ice floes in early October if the logistics support allows, because there is often a risk that the ice holes drilled for the equipment deployment are hard to refreeze, and the risk of floe fragmentation would increase by the end of ice melt season in August and September. In these situations, the equipment is prone to collapse, causing observation interruptions. As expected, the duration in both regions is longer in the case of disregarding the EEZs relative to that derived with the EEZ restriction. Even in the BG region, with a shorter duration of observation compared to that in the TPD region, the potential duration for Lagrangian observation is estimated to reach 255.4 days with the EEZs and 283.3 days without the EEZs, respectively, with the deployment on

508 November 1. This suggests that the deployment of buoys or camps on the floes in the central Arctic Ocean, even by the end

509 of October with the EEZ constraint, is still able to guarantee a observation duration of at least 8 months. Furthermore, the

510 influence of EEZ on the potential Lagrangian observation duration would gradually strengthen with later deployment dates.
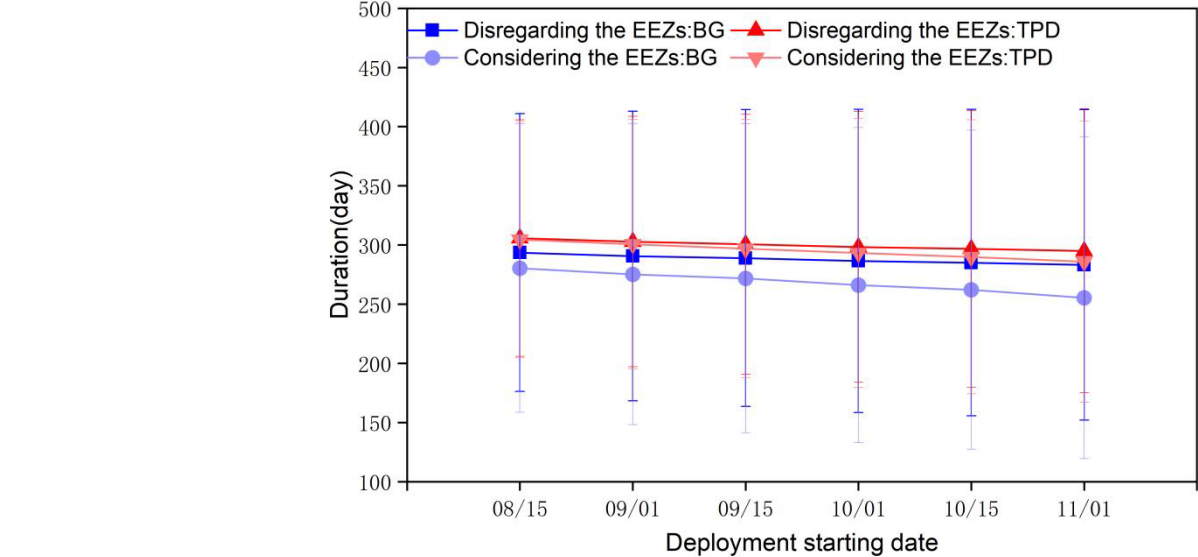

511

512 **Figure 12.** Changes in the mean duration of Lagrangian observations in 1979–2022 for various deployment dates from the starting points
513 reaching the BG or TPD region over 90% , for both cases of taking into account or disregarding the EEZs.

514 **5. Conclusions**

515 From a rectangular study region defined in the central Arctic Ocean excluding the EEZs, we reconstructed the sea ice

516 trajectories from 1979 to 2022 and determined the ideal deployment areas for the subsequent Lagrangian observations with a

517 an expected duration. On this basis, regional differences in the atmospheric conditions along the trajectories were assessed.

518 Subsequently, we explored the regulation mechanisms of atmospheric circulation patterns on sea ice advection and the

519 influence of EEZ boundary constraints and deployment time on the duration of sustained Lagrangian observation.

520 Deployment of Lagrangian observations at locations centered around 82°N and 160°E, near north of the East Siberian

521 and Laptev seas, can ensure at least 9 months of drifting observation time. The probabilities of remaining in the central

522 Arctic ice region during the 44-year study period ranges from 75.0% to 90.9%, with mainly moderate-recommendation zones

523 (75%–85%) with a spatial proportion of 80.4%, and small proportion of high-recommendation zones (>85%). Ice floes

524 originating from this area of 7.0×10^5 km^2 are more likely to reach the TPD region.

525 There are obvious regional differences in the atmospheric and sea ice conditions during ice drifting between the BG and

526 TPD regions. Near-surface (2 m) air temperatures in both regions of BG and TPD show a significant warming trend in 1979–

2022, with a higher increasing rate in the TPD region than in the BG region due to its proximity to the Atlantic sector of the Arctic Ocean. The significant decrease in FDD in the BG and TPD regions suggests that sea ice has experienced warmer conditions during the freezing season in recent years. Lagrangian observations in the TPD region would experience increased days of cloud opacity during the winter 1979–2022 by 19.4% compared to that in 1979–2006, because the cyclone activities are more frequent in the TPD region in recent years. The observations in the TPD region in early years would experience a relatively strong dynamic response of sea ice to wind forcing, with a higher ice-wind speed ratio than in the BG region. However, this response has been enhanced more prominently in the BG region due to the larger loss of multiyear ice, especially for the south part of BG region. Large-scale atmospheric circulation patterns at the early stage of ice drifting in autumn have a significant influence on the terminal location of ice trajectories. Thus, compared to the 1979–2022 average, the extreme positive phases of CAI and DA indices in autumn would expand the ideal deployment area to the Chukchi Sea and the Canada Basin. On the contrary, at the extreme negative phase of these indices, it is preferred to expand to the northern Laptev Sea.

In addition to natural conditions, the EEZ boundary has a great constraint on the Lagrangian observations. The absence of these constraints would increase the number of eligible starting points in the study region. Disregarding the EEZ boundary constraints, the eligible starting points with the trajectories toward the BG region expands southward, while for those toward the TPD region it would expand in the areas facing to the Fram Strait. The advanced deployment start time to mid August may result in a longer duration of Lagrangian observations, by 10.0 days compared to that obtained from the deployment on October 1. However, in order to reduce the failure risk of observation instruments deployed on the floes, in particular in the later ice melt season, we still consider the deployments in October are more appropriate for Lagrangian observation relying on ice floes in the central Arctic Ocean. Using the buoy data as a validation, the reconstructed trajectories have high geometrical similarity and accuracy, and the reconstruction in the BG region is better than that of the TPD region. Meanwhile, the accuracy of the Lagrangian method in ice trajectory reconstruction is higher than that of the semi-Lagrangian method, and the high-probability closure of the reconstructed forward and backward trajectories supports the high confidence of the reconstruction method.

In this study, daily SIM product is the main data source used to reconstruct sea ice drift trajectories and evaluate the ST of Lagrangian observations relying on ice floe. We acknowledge this as a primary evaluation, ignoring operational safety risks. The main challenges for survival and maintaining continuous observation for the specific devices deployed on the Arctic ice floes include the breakage or compression of sea ice, the formation of melt ponds, and the intrusion of polar bear, etc. As Arctic warming continues, the combined effects of accelerated melting and limited replenishment of multi-year ice will eventually trigger the complete loss of multiyear ice and a shift to a seasonally ice-free Arctic ocean (Babb et al., 2023).

This change puts forward greater demands on ice floe-based observational campaigns and on the development of more adaptive observational techniques and equipment to cope with future extreme ice and atmospheric environments. Our work mainly provides supporting cognition for the site selection for the deployments of ice buoy and ice camp. The preferred areas identified in this study still require adaptable adjustments, associated with the changes in Arctic sea ice itself in the future. From a practical perspective, once reaching the preferred deployment area, the specific conditions of the ice floe, such as ice thickness, floe size, and distribution of ice ridge and melt pond, need to be further surveyed using high resolution satellite remote sensing images and helicopters or ice-based measurements.

Appendix

Table A1. Basic information on buoy data used for validation of reconstructed ice drift trajectories

Number	Start date (YY/MM/DD)	Start location (°N, °E)	End Date (YY/MM/DD)	End location (°N, °E)	Duration (Day)	Buoys type
1	18/10/01	78.49, -146.12	19/08/24	71.29, -133.35	328	Snow_Buoy
2	20/11/04	83.93, -149.12	20/12/30	82.53, -144.07	57	iSVP
3	20/11/04	83.77, -110.26	20/12/30	82.81, -115.35	57	iSVP
4	20/11/04	82.50, -160.67	20/12/30	81.18, -154.30	57	iSVP
5	20/10/01	79.12, -140.50	20/12/26	76.66, -141.98	87	ITP
6	18/08/13	81.19, -169.34	19/02/27	80.88, -134.24	199	SIMBA
7	14/09/01	77.96, -141.98	15/05/24	75.67, -151.84	266	iSVP
8	14/09/01	81.32, -156.03	15/08/31	77.85, -138.64	365	iSVP
9	14/09/01	78.24, -162.07	15/08/31	79.50, -151.95	365	iSVP
10	16/09/01	82.67, -142.03	16/12/31	77.99, -132.51	122	iSVP
11	12/06/29	75.34, -165.97	12/08/08	77.74, -159.63	41	ITP
12	21/08/25	75.00, -149.90	21/09/09	75.67, -146.56	16	AXIB
13	14/09/12	79.99, -167.96	15/09/03	81.36, -160.42	356	-

14	22/07/14	74.61, -162.14	22/08/11	75.21, -162.29	29	IceCadet
15	11/08/05	78.01, -139.94	11/10/21	78.84, -134.63	76	-
16	15/10/01	85.06, 136.82	16/09/30	83.28, 8.21	366	PAWS
17	15/10/01	84.46, 115.64	16/09/12	81.13, 5.95	330	iSVP
18	15/10/01	85.06, 136.92	16/09/30	83.27, 8.20	366	Snow_Buoy
19	18/10/01	82.63, 141.50	19/08/26	82.42, 11.34	330	iSVP
20	18/10/01	81.17, 159.90	19/08/24	87.18, 13.64	328	Snow_Buoy
21	19/10/01	82.62, 120.56	20/09/29	83.30, 8.73	364	iSVP
22	19/10/01	86.18, 125.61	20/06/08	81.05, 3.78	252	iSVP
23	19/10/10	85.13, 133.02	20/07/14	81.04, -0.10	279	SIMBA
24	19/10/01	85.71, 123.25	20/07/14	81.06, -0.67	288	SVP5S 003
25	19/03/26	86.90, 94.19	19/12/08	81.11, 4.56	258	iSVP
26	10/04/19	88.69, 145.18	10/07/29	87.51, -0.59	102	AOFB
27	11/09/09	84.79, 165.96	11/12/17	85.29,-162.785	100	ITP
28	13/01/11	85.49, 125.51	13/08/22	85.47, 29.31	224	ITP
29	23/08/31	84.93, 129.60	23/12/31	86.01, 104.04	123	Thermistor String
30	12/12/01	82.98, 129.08	13/08/15	86.58, 20.20	255	SIMB
31	97/10/01	75.10, -140.83	98/06/30	78.03, -164.63	273	IOEB
32	07/04/23	86.12, 144.92	07/11/14	85.33, -9.45	206	CALIB

566   Note: buoys without specified types indicate that the IABP does not provide information on the buoy type.
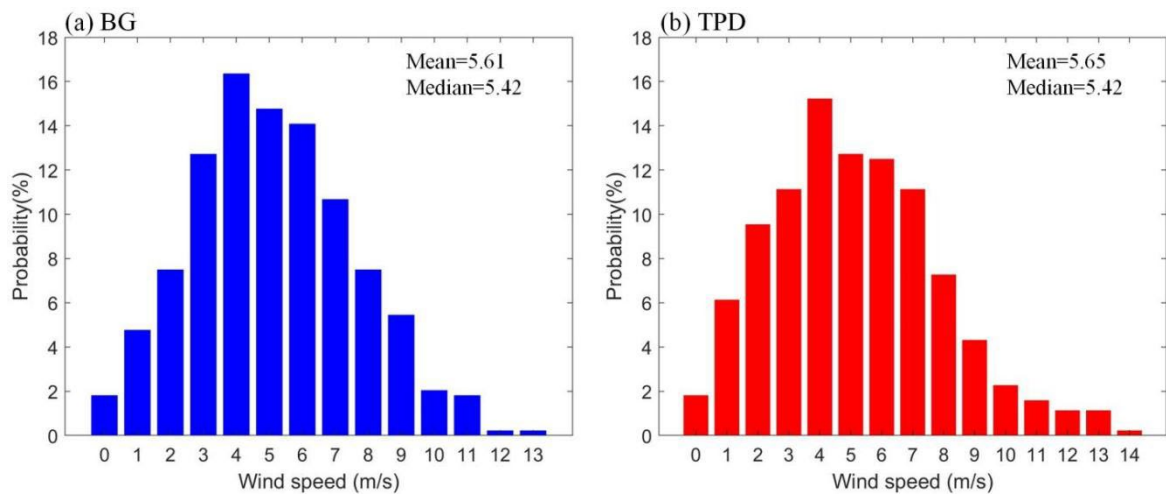
Figure A1 Probability distribution of wind speed in the initial 10 days along the reconstructed trajectories in the BG and TPD regions in 1979–2022.

Data Availability

Sea ice motion, concentration data from NSIDC is available at https://nsidc.org/data/NSIDC-0116/versions/4.and https://nsidc.org/data/G02202/versions/4. Sea ice thickness data is downloaded from https://data.seaiceportal.de/data/cs2smos_awi/v204/. Shapefiles of maritime boundaries and EEZs are publicly available online (https://www.marineregions.org/). The ERA5 reanalysis data are downloaded from https://cds.climate.copernicus.eu/cdsapp#!/dataset/reanalysis-era5-single-levels. Buoy data is available at https://www.meereisportal.de/, https://iabp.apl.uw.edu/TABLES/ArcticTable.html, and https://www.wdc-climate.de/ui/.

Financial support

Competing interests

The contact author has declared that none of the authors has any competing interests.

Reference

Babb, D.G., Galley, R.J., Kirillov, S., Landy, J.C., Howell, S.E.L., Stroeve, J.C., Meier, W., Ehn, J.K., and Barber, D.G., 2023. The

585   Stepwise Reduction of Multiyear Sea Ice Area in the Arctic Ocean Since 1980. J. Geophys. Res. Ocean, 128(10),
586   https://doi.org/10.1029/2023JC020157.

587   Batrak, Y., and Müller, M., 2019. On the warm bias in atmospheric reanalyses induced by the missing snow over Arctic sea-ice. Nat.
588   Commun, 10(1), 4170, https://doi.org/10.1038/s41467-019-11975-3.

589   Bigdeli, A., Nguyen, A.T., Pillar, H.R., Ocaña, V. and Heimbach, P., 2020. Atmospheric Warming Drives Growth in Arctic Sea Ice: A Key
590   Role for Snow. Geophys. Res. Lett, 47(20): e2020GL090236, https://doi.org/10.1029/2020GL090236.

591   Brümmer, B., Müller, G., Haller, M., Kriegsmann, A., Offermann, M., and Wetzel, C, 2011. DAMOCLES 2007–2008– Hamburg Arctic
592   Ocean buoy drift experiment: meteorological measurements of 16 autonomous drifting ice buoys.
593   https://doi.org/10.1594/WDCC/UNI_HH_MI_ DAMOCLES2007

594   Cabaniss, G.H., Hunkins, K.L., and Untersteiner, N., 1965. US-IGY Drifting Station Alpha, Arctic Ocean 1957-1958, Special Reports. Air
595   Force Cambridge Research Laboratories, No. 38, Bedford, MA, p. 322.

596   Cohen, J., Zhang, X., Francis, J. and coauthors, 2020. Divergent consensuses on Arctic amplification influence on midlatitude severe
597   winter weather. Nat. Clim. Chang. 10, 20–29. https://doi.org/10.1038/s41558-019-0662-y.

598   Coon, M.D., 1980. A review of AIDJEX modeling, in: Pritchard, R.S. (Ed.), Sea Ice Processes and Models: Symposium Proceedings. Univ.
599   of Wash. Press, Seattle, pp. 12 – 27.

600   Cox, C.J., and Coauthors, 2023. Continuous observations of the surface energy budget and meteorology over the Arctic sea ice during
601   MOSAiC. Sci. Data, 10(1), 519, https://doi.org/10.1038/s41597-023-02415-5.

602   Devogele, T., L. Etienne, M. Esnault, and F. Lardy., 2017. Optimized discrete Fréchet distance between trajectories. Proceedings of the 6th
603   ACM SIGSPATIAL Workshop on Analytics for Big Geospatial Data, 11–19. Redondo Beach, USA. CA.
604   https://doi.org/10.1145/3150919.3150924.

605   Fang, Y., Wang, X., Li, G., Chen, Z., Hui, F., and Cheng, X., 2023. Arctic sea ice drift fields extraction based on feature tracking to
606   MODIS imagery. Int. J. Appl. Earth. Obs, 120, 103353, https://doi.org/10.1016/j.jag.2023.103353.

607   Flanders Marine Institute (2023). Maritime Boundaries Geodatabase, version 12. Available online at https://www.marineregions.org/.
608   https://doi.org/10.14284/628.

609   Feng, J., Zhang, Y., Cheng, Q., Wong, K., Li, Y., and Yeu Tsou, J., 2021. Effect of melt ponds fraction on sea ice anomalies in the Arctic
610   Ocean. Int. J. Appl. Earth. Obs, 98, 102297, https://doi.org/10.1016/j.jag.2021.102297.

611   Frolov, I.E., 2005. The arctic basin : results from the Russian drifting stations. Springer, Berlin, Germany.

612   Goosse, H., and Coauthors, 2018. Quantifying climate feedbacks in polar regions. Nat. Commun, 9(1), 1919,
613   https://doi.org/10.1038/s41467-018-04173-0.

614   Graham, R.M., Cohen, L., Ritzhaupt, N., Segger, B., Graversen, R.G., Rinke, A., Walden, V.P., Granskog, M.A., and Hudson, S.R., 2019a.
615   Evaluation of Six Atmospheric Reanalyses over Arctic Sea Ice from Winter to Early Summer. J. Climate, 32(14), 4121-4143,
616   https://doi.org/10.1175/JCLI-D-18-0643.1.

617   Graham, R.M., Hudson, S.R., and Maturilli, M., 2019b. Improved Performance of ERA5 in Arctic Gateway Relative to Four Global
618   Atmospheric Reanalyses. Geophys. Res. Lett, 46(11), 6138-6147, https://doi.org/10.1029/2019GL082781.

619   Graham, R.M., Rinke, A., Cohen, L., Hudson, S.R., Walden, V.P., Granskog, M.A., Dorn, W., Kayser, M., and Maturilli, M., 2017. A
620   comparison of the two Arctic atmospheric winter states observed during N-ICE2015 and SHEBA. J. Geophys. Res. Atmos, 122(11),
621   5716-5737, https://doi.org/10.1002/2016JD025475.

622   Granskog, M., Assmy, P., Gerland, S., Spreen, G., Steen, H., and Smedsrud, L.J.E., 2016. Arctic research on thin ice: Consequences of
623   Arctic sea ice loss. Eos, 97(5), 22-26, https://doi.org/10.1029/2016EO044097.

624   Gui, D., Lei, R., Pang, X., Hutchings, J.K., Zuo, G., and Zhai, M., 2020. Validation of remote-sensing products of sea-ice motion: a case
625   study in the western Arctic Ocean. J. Glaciol, 66(259), 807-821, https://doi.org/10.1017/jog.2020.49.

626   Haller, M., Brümmer, B., and Müller, G., 2014. Atmosphere-ice forcing in the transpolar drift stream: results from the DAMOCLES
627   ice-buoy campaigns 2007-2009. Cryosphere, 8(1), 275-288, https://doi.org/10.5194/tc-8-275-2014.

628   Herman, A., and Glowacki, O., 2012. Variability of sea ice deformation rates in the Arctic and their relationship with basin-scale wind
629   forcing. Cryosphere, 6(6), 1553-1559, https://doi.org/10.5194/tc-6-1553-2012.

630   Hersbach, H., and Coauthors, 2020. The ERA5 global reanalysis. Q. J, Roy. Meteor. Soc, 146(730), 1999-2049,
631   https://doi.org/10.1002/qj.3803.

632   Holland, M.M., and E.C. Hunke. 2022. A review of Arctic sea ice climate predictability in large-scale Earth system models. Oceanography
633   35(3–4):20–27, https://doi.org/10.5670/oceanog.2022.113.

634   Jackson, K., Wilkinson, J., Maksym, T., Meldrum, D., Beckers, J., Haas, C., and Mackenzie, D., 2013. A Novel and Low-Cost Sea Ice
635   Mass Balance Buoy. J. Atos. Ocean. Tech, 30(11), 2676-2688, https://doi.org/10.1175/JTECH-D-13-00058.1.

636   Koo, Y., Lei, R.B., Cheng, Y.B., Cheng, B., Xie, H.J., Hoppmann, M., Kurtz, N.T., Ackley, S.F., and Mestas-Nuñez, A.M., 2021.
637   Estimation of thermodynamic and dynamic contributions to sea ice growth in the Central Arctic using ICESat-2 and MOSAiC
638   SIMBA buoy data. Remote. Sens. Environ, 267, https://doi.org/10.1016/j.rse.2021.112730.

639   Krumpen, T., Belter, H.J., Boetius, A., et al, 2019. Arctic warming interrupts the Transpolar Drift and affects long-range transport of sea ice
640   and ice-rafted matter. Sci. Rep, 9(1), https://doi.org/10.1038/s41598-019-41456-y.

641   Krumpen, T., and Coauthors, 2020. The MOSAiC ice floe: sediment-laden survivor from the Siberian shelf. Cryosphere, 14(7), 2173-2187,
642   https://doi.org/10.5194/tc-14-2173-2020.

643   Krumpen, T., and Coauthors, 2021. MOSAiC drift expedition from October 2019 to July 2020: sea ice conditions from space and
644   comparison with previous years. Cryosphere, 15(8), 3897-3920, https://doi.org/10.5194/tc-15-3897-2021.

645   Kwok, R., 2018. Arctic sea ice thickness, volume, and multiyear ice coverage: losses and coupled variability (1958-2018). Environmental
646   Research Letters, 13(10), https://doi.org/10.1088/1748-9326/aae3ec.

647   Kwok, R., Spreen, G., and Pang, S., 2013. Arctic sea ice circulation and drift speed: Decadal trends and ocean currents. J. Geophys. Res.
648   Ocean, 118(5), 2408-2425, https://doi.org/10.1002/jgrc.20191.

649   Lavergne, T., Eastwood, S., Teffah, Z., Schyberg, H., and Breivik, L.A., 2010. Sea ice motion from low-resolution satellite sensors: An
650   alternative method and its validation in the Arctic. J. Geophys. Res. Ocean, 115(C10), https://doi.org/10.1029/2009JC005958.

651   Lavergne, T., and Coauthors, 2019. Version 2 of the EUMETSAT OSI SAF and ESA CCI sea-ice concentration climate data records.
652   Cryosphere, 13(1), 49-78, https://doi.org/10.5194/tc-13-49-2019.

653   Lei, R., and Coauthors, 2022. Seasonality and timing of sea ice mass balance and heat fluxes in the Arctic transpolar drift during 2019–
654   2020. Elementa-Sci. Anthrop, 10(1), 000089, https://doi.org/10.1525/elementa.2021.000089.

655   Lei, R., Gui, D., Hutchings, J.K., Wang, J., and Pang, X., 2019. Backward and forward drift trajectories of sea ice in the northwestern
656   Arctic Ocean in response to changing atmospheric circulation. Int. J. Climatol, 39(11), 4372-4391, https://doi.org/10.1002/joc.6080.

657   Leppäranta, M., 1993. A review of analytical models of sea-ice growth. Atmos. Ocean, 31(1), 123-138,
658   https://doi.org/10.1080/07055900.1993.9649465.

659   Leppäranta, M., 2011. The Drift of Sea Ice. Springer Berlin, Heidelberg.

660   Li, M., Zhou, C., Chen, X., Liu, Y., Li, B., and Liu, T., 2022. Improvement of the feature tracking and patter matching algorithm for sea ice
661   motion retrieval from SAR and optical imagery. Int. J. Appl. Earth. Obs, 112, 102908, https://doi.org/10.1016/j.jag.2022.102908.

662   Lindsay, R.W., 2002. Ice deformation near SHEBA. J. Geophys. Res. Ocean, 107(C10), https://doi.org/10.1029/2000JC000445.

663   Liu, J.P., and Coauthors, 2019. Towards reliable Arctic sea ice prediction using multivariate data assimilation. Sci. Bull, 64(1), 63-72,
664   https://doi.org/10.1016/j.scib.2018.11.018.

665   Lukovich, J.V., Babb, D.G., and Barber, D.G., 2011. On the scaling laws derived from ice beacon trajectories in the southern Beaufort Sea
666   during the International Polar Year - Circumpolar Flaw Lead study, 2007–2008. J. Geophys. Res. Ocean, 116(C9),
667   https://doi.org/10.1029/2011JC007049.

668   Lund-Hansen, L.C., Søgaard, D.H., Sorrell, B.K., Gradinger, R., and Meiners, K.M., 2020. Autumn, development and consolidation of sea
669   ice, in: Lund-Hansen, L.C., Søgaard, Dorte H., Sorrell, B.K., Gradinger, R., Meiners, K.M. (Eds.), Arctic Sea Ice Ecology: Seasonal
670   Dynamics in Algal and Bacterial Productivity. Springer International Publishing, Cham, pp. 13-30.

671   Markus, T., Stroeve, J.C., and Miller, J., 2009. Recent changes in Arctic sea ice melt onset, freezeup, and melt season length. J. Geophys.
672   Res. Ocean, 114(C12), https://doi.org/10.1029/2009JC005436.

673   Meier, W.N., and Stroeve, J., 2022. An Updated Assessment of the Changing Arctic Sea Ice Cover. Oceanography, 35(3-4), 10-19,
674   https://doi.org/10.5670/oceanog.2022.114.

675   Moore, G.W.K., Schweiger, A., Zhang, J., and Steele, M., 2018. Collapse of the 2017 Winter Beaufort High: A Response to Thinning Sea
676   Ice? Geophys. Res. Lett, 45(6), 2860-2869, https://doi.org/10.1002/2017gl076446.

677   Morison, J., and Coauthors, 2002. North Pole Environmental Observatory delivers early results. Eos, 83(33), 357-361,
678   https://doi.org/10.1029/2002EO000259.

679   Nicolaus, M., Hoppmann, M., Arndt, S., Hendricks, S., Katlein, C., Nicolaus, A., Rossmann, L., Schiller, M., and Schwegmann, S., 2021.
680   Snow Depth and Air Temperature Seasonality on Sea Ice Derived From Snow Buoy Measurements. Front. Mar. Sci, 8,
681   https://doi.org/10.3389/fmars.2021.655446.

682   Nicolaus, M., and Coauthors, 2022. Overview of the MOSAiC expedition: Snow and sea ice. Elementa-Sci. Anthrop, 10(1),
683   https://doi.org/10.1525/elementa.2021.000046.

684   Parkinson, C.L., and DiGirolamo, N.E., 2021. Sea ice extents continue to set new records: Arctic, Antarctic, and global results. Remote.
685   Sens. Environ, 267, 112753, https://doi.org/10.1016/j.rse.2021.112753.

686   Pithan, F., Athanase, M., Dahlke, S., Sánchez-Benítez, A., Shupe, M.D., Sledd, A., Streffing, J., Svensson, G., and Jung, T., 2023. Nudging
687   allows direct evaluation of coupled climate models with in situ observations: a case study from the MOSAiC expedition. Geosci.
688   Model. Dev, 16(7), 1857-1873, https://doi.org/10.5194/gmd-16-1857-2023.

689   Proshutinsky, A., Bourke, R.H., and McLaughlin, F.A., 2002. The role of the Beaufort Gyre in Arctic climate variability: Seasonal to
690   decadal climate scales. Geophys. Res. Lett, 29(23), 15-11-15-14, https://doi.org/10.1029/2002GL015847.

691   Proshutinsky, A.Y., and Johnson, M.A., 1997. Two circulation regimes of the wind-driven Arctic Ocean. J. Geophys. Res. Ocean, 102(C6),
692   12493-12514, https://doi.org/10.1029/97JC00738.

693   Rabe, B., and Coauthors, 2024. The MOSAiC Distributed Network: Observing the coupled Arctic system with multidisciplinary,
694   coordinated platforms. Elementa-Sci. Anthrop, 12(1), 00103, https://doi.org/10.1525/elementa.2023.00103.

695   Rabe, B., and Coauthors, 2022. Overview of the MOSAiC expedition: Physical oceanography. Elementa-Sci. Anthrop, 10(1),
696   https://doi.org/10.1525/elementa.2021.00062.

697   Rantanen, M., Karpechko, A.Y., Lipponen, A., Nordling, K., Hyvärinen, O., Ruosteenoja, K., Vihma, T., and Laaksonen, A., 2022. The
698   Arctic has warmed nearly four times faster than the globe since 1979. Commun. Earth. Environ, 3(1), 168,
699   https://doi.org/10.1038/s43247-022-00498-3.

700   Richter-Menge, J.A., Perovich, D.K., Elder, B.C., Claffey, K., Rigor, I., and Ortmeyer, M., 2006. Ice mass-balance buoys: a tool for
701   measuring and attributing changes in the thickness of the Arctic sea-ice cover. Ann. Glaciol, 44, 205-210,
702   https://doi.org/10.3189/172756406781811727.

703   Ricker, R., Hendricks, S., Girard-Ardhuin, F., Kaleschke, L., Lique, C., Tian-Kunze, X., Nicolaus, M., and Krumpen, T., 2017a.
704   Satellite-observed drop of Arctic sea ice growth in winter 2015–2016. Geophys. Res. Lett, 44(7), 3236-3245,
705   https://doi.org/10.1002/2016GL072244.

706   Ricker, R., Hendricks, S., Kaleschke, L., Tian-Kunze, X., King, J., and Haas, C.J.T.C., 2017b. A weekly Arctic sea-ice thickness data
707   record from merged CryoSat-2 and SMOS satellite data. Cryosphere, 11(4), 1607-1623, https://doi.org/10.5194/tc-11-1607-2017.

708   Rigor, I.G., Wallace, J.M., and Colony, R.L., 2002. Response of sea ice to the Arctic Oscillation. J. Climate, 15(18), 2648-2663,
709   https://doi.org/10.1175/1520-0442(2002)0152.0.CO;2.

710   Rinke, A., Cassano, J.J., Cassano, E.N., Jaiser, R., and Handorf, D., 2021. Meteorological conditions during the MOSAiC expedition:
711   Normal or anomalous? Elementa-Sci. Anthrop, 9(1), https://doi.org/10.1525/elementa.2021.00023.

712   Robinson, A., Lehmann, J., Barriopedro, D., Rahmstorf, S., and Coumou, D., 2021. Increasing heat and rainfall extremes now far outside
713   the historical climate. Npj. Clim. Atmos. Sci, 4(1), 45, https://doi.org/10.1038/s41612-021-00202-w.

714   Sagawa, G. and Yamaguchi, H. 2006. A Semi-Lagrangian Sea Ice Model For High Resolution Simulation. The Sixteenth International
715   Offshore and Polar Engineering Conference. San Francisco, California, USA.

716   Shaw, W.J., Stanton, T.P., McPhee, M.G., and Kikuchi, T., 2008. Estimates of surface roughness length in heterogeneous under-ice
717   boundary layers. J. Geophys. Res. Ocean, 113(C8), https://doi.org/10.1029/2007JC004550.

718   Shupe, M.D., and Coauthors, 2022. Overview of the MOSAiC expedition-Atmosphere INTRODUCTION. Elementa-Sci. Anthrop, 10(1),
719   https://doi.org/10.1525/elementa.2021.00060.

Smith, M.M., Holland, M., and Light, B., 2022. Arctic sea ice sensitivity to lateral melting representation in a coupled climate model. Cryosphere, 16(2), 419-434, https://doi.org/10.5194/tc-16-419-2022.

Subich, C., Pellerin, P., Smith, G. and Dupont, F., 2020. Development of a semi-Lagrangian advection scheme for the NEMO ocean model (3.1). Geosci. Model. Dev, 13(9): 4379-4398, https://doi.org/10.5194/gmd-13-4379-2020.

Sumata, H., de Steur, L., Divine, D.V., Granskog, M.A., and Gerland, S., 2023. Regime shift in Arctic Ocean sea ice thickness. Nature, 615(7952), 443-449, https://doi.org/10.1038/s41586-022-05686-x.

Thompson, D.W.J., and Wallace, J.M., 1998. The Arctic Oscillation signature in the wintertime geopotential height and temperature fields. Geophys. Res. Lett, 25(9), 1297-1300, https://doi.org/10.1029/98gl00950.

Tian, T., Yang, S., Høyer, J.L., Nielsen-Englyst, P., and Singha, S., 2024. Cooler Arctic surface temperatures simulated by climate models are closer to satellite-based data than the ERA5 reanalysis. Commun. Earth. Environ, 5(1), 111, https://doi.org/10.1038/s43247-024-01276-z.

Toole, J.M., Curry, R.G., Joyce, T.M., McCartney, M., and Peña-Molino, B., 2011. Transport of the North Atlantic Deep Western Boundary Current about 39°N, 70°W: 2004–2008. Deep-Sea. Res Pt II, 58(17), 1768-1780, https://doi.org/10.1016/j.dsr2.2010.10.058.

Tschudi, M. A., Fowler, C., Maslanik, J. A., and Stroeve, J.C., 2010. Tracking the movement and changing surface characteristics of Arctic sea ice. IEEE J. Sel. Topics Appl. Earth Observ. Remote Sens., 3, 536–540, https://doi.org/10.1109/JSTARS.2010.2048305.

Tschudi, M. A,, Meier, W. N., Stewart, J. S., Fowler, C., and Maslanik, J.: Polar Pathfinder Daily 25 km EASE-Grid Sea Ice Motion Vectors, Version 4, Boulder, NASA National Snow and Ice Data Center Distributed Active Archive Center, Colorado USA, [data set], https://doi.org/10.5067/INAWUWO7QH7B, 2019.

Tschudi, M.A., Meier, W.N., and Stewart, J.S., 2020. An enhancement to sea ice motion and age products at the National Snow and Ice Data Center (NSIDC). Cryosphere, 14(5), 1519-1536, https://doi.org/10.5194/tc-14-1519-2020.

Uttal, T., and Coauthors, 2002. Surface Heat Budget of the Arctic Ocean. B. Am. Meteorol. Soc, 83, 255-275,

Vautard, R., and Coauthors, 2013. The simulation of European heat waves from an ensemble of regional climate models within the EURO-CORDEX project. Clim. Dynam, 41(9), 2555-2575, https://doi.org/10.1007/s00382-013-1714-z.

Vihma, T., Tisler, P., and Uotila, P., 2012. Atmospheric forcing on the drift of Arctic sea ice in 1989-2009. Geophys. Res. Lett, 39, https://doi.org/10.1029/2011gl050118.

Wang, C., Graham, R.M., Wang, K., Gerland, S. and Granskog, M.A, 2019. Comparison of ERA5 and ERA-Interim near-surface air temperature, snowfall and precipitation over Arctic sea ice: effects on sea ice thermodynamics and evolution. Cryosphere, 13(6): 1661-1679, https://doi.org/10.5194/tc-13-1661-2019.

Wang, J., Zhang, J., Watanabe, E., Ikeda, M., Mizobata, K., Walsh, J.E., Bai, X., and Wu, B., 2009. Is the Dipole Anomaly a major driver to record lows in Arctic summer sea ice extent? Geophys. Res. Lett, 36(5), https://doi.org/10.1029/2008GL036706.

Wu, B.Y., Wang, J., and Walsh, J.E., 2006. Dipole anomaly in the winter Arctic atmosphere and its association with sea ice motion. J. Climate, 19(2), 210-225, https://doi.org/10.1175/JCLI3619.1.

Zhang, X., Tang, H., Zhang, J., Walsh, J.E., Roesler, E.L., Hillman, B., Ballinger, T.J., and Weijer, W., 2023. Arctic cyclones have become more intense and longer-lived over the past seven decades. Commun. Earth. Environ, 4(1), 348, https://doi.org/10.1038/s43247-023-01003-0.